وزارة البحث العلمي والتعليم العالي

MINISTERE DE L'ENSEIGNEMENT SUPÉRIEUR ET DE LA RECHERCHE SCIENTIFIQUE

جامعـة عبد الحميد بن باديس مستغانم

UNIVERSITÉ ABDELHAMID IBN BADIS MOSTAGANEM

كـليـة الـعـلـوم والـتكـنـولـوجيـا

FACULTÉ DES SCIENCES ET DE LA TECHNOLOGIE

DEPARTEMENT DE GENIE ELECTRIQUE

MEMOIRE

Présenté pour obtenir le diplôme de
Master académique

MASTER EN ÉLECTROTECHNIQUE

Option : Énergies renouvelables en électrotechnique

Par

Bouziane Farouk Mohamed

Subject :

Maintenance of Photovoltaic Systems in Arid and Semi-Arid Climates and Design of an Automatic solar panel Cleaning Robot

Encadreur : Dr. Ghomri. Leila

jury :
Dr. Benyamina Mansour
Dr. Benzidane Mohamed Reda

Année Universitaire 2025/2026

Gratitude

First and foremost, I thank ALLAH the Almighty for giving me the courage, the will and the patience to complete this work.

I would like to express my sincere gratitude to my supervisor, Professor Leila Ghomri, for her unwavering support, encouragement, competence, and constructive criticism which helped shape this work into something I am truly proud of.
I would also like to extend my sincere thanks to the members of the jury, Dr. Benyamina Mansour and Dr. Benzidane Mohamed Reda for accepting to evaluate my work and for the time and effort they have devoted to its assessment

I would also like to extend my sincere thanks to Mr. Djafni Djamel, Engineer at Ahmed Ben Bella airport, for his guidance, support, and valuable insights during my internship. His assistance contributed to my practical understanding and enriched my learning experience.

Finally, I would like to express my deepest appreciation to all the professors who contributed to my education throughout my university journey at Abdelhamid Ibn Badis University.
Their guidance, dedication, and knowledge have played a fundamental role in my academic development, and this work would not have been possible without their support.

Dedication

I dedicate this work to my parents, the two most important people in my life. Their unwavering support throughout my journey, through both my successes and challenges, has helped shape me into the person I am today. Without their love, guidance, and encouragement, I would be lost. To my mother, who stayed up late praying for my success, and to my father, who sacrificed so much to ensure that I had every opportunity to achieve my goals, I offer my deepest gratitude and love.

To my siblings, who continually inspire me and encourage me to become a better person every day, thank you for your constant support and motivation.

To my extended family, whose encouragement and support have reached me from across the country, I am sincerely grateful for your kindness and belief in me.

To all the dear friends I have made throughout my school and university years, thank you for the memories, companionship, and support that have made this journey more meaningful and enjoyable.

Finally, I dedicate this work to my five classmates, with whom I have shared countless challenges, experiences, and achievements. I hope we graduate together and move forward toward bright and successful futures. I wish each of us happiness, success, and fulfillment in the years to come.

Table of Contents

Abstract

In this work, the impact of maintenance on the performance and lifetime of photovoltaic systems installed in arid and semi-arid climates is investigated. Studies [1] show that dust accumulation on photovoltaic modules causes significant power losses, especially in desert regions where soiling rates are high. Research in Renewable and Sustainable Energy Reviews confirms that regular cleaning is necessary to maintain energy production and system efficiency.

This study examines the use of cleaning as well as a showcase of a robot for solar panel cleaning.

The main contribution of this work is the design of a robotic cleaning system. The proposed system aims to reduce manual labor, minimize water consumption, and improve cleaning efficiency in large scale photovoltaic installations as well as a design for a cheap system.

A technical discussion comparing systems with regular maintenance and systems without planned maintenance is presented. The results emphasize the importance of preventive strategies in maintaining energy yield and extending system lifetime.

Résumé

Dans ce travail, l'impact de la maintenance sur la performance et la durée de vie des systèmes photovoltaïques installés dans des climats arides et semi-arides est étudié. Des études [1] montrent que l'accumulation de poussière sur les modules photovoltaïques entraîne des pertes de puissance importantes, en particulier dans les régions désertiques où les taux d'encrassement sont élevés. Des recherches publiées dans Renewable and Sustainable Energy Reviews confirment que le nettoyage régulier est nécessaire pour maintenir la production d'énergie et l'efficacité du système.

Cette étude examine l'utilisation du nettoyage ainsi qu'une présentation d'un robot dédié au nettoyage des panneaux solaires.

La principale contribution de ce travail est la conception d'un système robotisé de nettoyage. Le système proposé vise à réduire le travail manuel, minimiser la consommation d'eau et améliorer l'efficacité du nettoyage dans les installations photovoltaïques à grande échelle, ainsi qu'à proposer une conception à faible coût.

Une discussion technique comparant les systèmes avec maintenance régulière et ceux sans maintenance planifiée est présentée. Les résultats soulignent l'importance des stratégies préventives pour maintenir le rendement énergétique et prolonger la durée de vie du système.

الملخص

في هذا العمل، يتم دراسة تأثير الصيانة على أداء وعمر الأنظمة الكهروضوئية المثبتة في المناخات الجافة وشبه الجافة. تُظهر الدراسات [1] أن تراكم الغبار على الألواح الكهروضوئية يؤدي إلى خسائر كبيرة في القدرة المنتجة، خاصة في المناطق الصحراوية حيث تكون معدلات . تؤكد الأبحاث المنشورة في مجلة
Renewable and Sustainable Energy Reviews
أن التنظيف المنتظم ضروري للحفاظ على إنتاج الطاقة وكفاءة النظام.

تتناول هذه الدراسة استخدام عمليات التنظيف بالإضافة إلى عرض روبوت مخصص لتنظيف الألواح الشمسية.

تتمثل المساهمة الرئيسية لهذا العمل في تصميم نظام روبوتي للتنظيف. يهدف النظام المقترح إلى تقليل العمل اليدوي، وتقليل استهلاك المياه، وتحسين كفاءة التنظيف في محطات الطاقة الشمسية واسعة النطاق، إضافة إلى تصميم منخفض التكلفة.

كما يتم تقديم مناقشة تقنية تقارن بين الأنظمة ذات الصيانة المنتظمة وتلك التي تعمل دون صيانة مخططة. وتؤكد النتائج أهمية استراتيجيات الصيانة الوقائية للحفاظ على إنتاج الطاقة وإطالة عمر النظام.

General Introduction

The increasing global demand for energy, combined with environmental concerns related to fossil fuel consumption, has accelerated the development of renewable energy technologies. According to the International Energy Agency, renewable energy sources are playing a growing role in global electricity production, with solar photovoltaic technology being one of the fastest expanding sectors. Photovoltaic systems are considered a clean and sustainable solution for electricity generation because they produce no direct greenhouse gas emissions during operation.

In arid and semi-arid regions, such as North Africa and the Middle East, solar energy presents a significant opportunity due to high solar irradiance levels. However, environmental conditions such as dust accumulation, high temperature, and sandstorms negatively affect photovoltaic system performance. Several studies [2] published in Renewable and Sustainable Energy Reviews journal report that soiling caused by dust deposition can significantly reduce the energy output of photovoltaic modules if regular cleaning is not performed.

In addition to surface soiling, photovoltaic systems are also affected by aging of electrical components. Reports from the National Renewable Energy Laboratory indicate that inverter failures are among the most common causes of system downtime. High temperature operation accelerates the degradation of internal components such as electrolytic capacitors, which reduces system reliability and lifetime.

For these reasons, maintenance plays a critical role in ensuring stable energy production, improving system efficiency, and extending the lifetime of panels

The objective of this work is to study the impact of preventive maintenance on photovoltaic system performance in arid climates. Special attention is given to cleaning strategies and component reliability. A robotic cleaning system is designed, in order to improve cleaning efficiency and reduce manual intervention.

This work is structured as follows. The first chapter presents a general overview of photovoltaic systems and their operating principles. The second chapter discusses common degradation mechanisms and maintenance requirements in photovoltaic installations. The third chapter presents the design and operating principle of the proposed robotic cleaning system. The final chapter provides a technical discussion on maintenance optimization and its impact on system performance and reliability. The study concludes with a general conclusion

CHAPTER 1
General Overview of Photovoltaic Solar Energy

1.1 Renewable Energy and Solar Power

Energy is essential for modern life, including industry, transportation, and residential use. The majority of global energy is still produced from fossil fuels such as oil, coal, and natural gas, which contribute to greenhouse gas emissions and climate change. Renewable energy sources are clean and abundant alternatives that help reduce environmental impact. Among the renewable sources, solar energy is one of the most widely available worldwide.

Solar energy comes from the sun as electromagnetic radiation. It is considered a clean and almost limitless source of energy compared with fossil fuels. Photovoltaic (PV) technology is a way to convert sunlight directly into electricity through electronic processes in materials known as semiconductors.

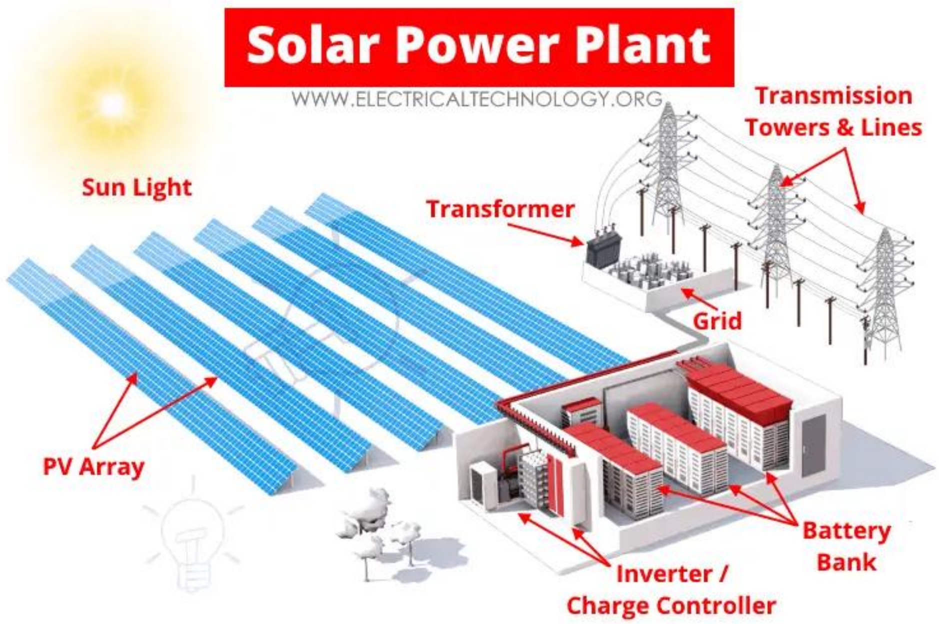

Figure 1: General structure of a solar power plant [3]

1.2 Photovoltaic Effect and Solar Cells

The photovoltaic effect was discovered in the 19th century and is the fundamental principle behind solar cells. When sunlight hits certain materials, it excites electrons and generates a flow of electric current. A single solar cell can produce a small amount of electrical power. To obtain practical power levels, many cells are connected in modules known as solar panels.

Solar cells are typically made from semiconductor materials such as crystalline silicon. These materials absorb sunlight and convert it into direct current (DC) electricity. Multiple solar panels can be combined into arrays to increase the total power output for residential, commercial, or utility-scale applications. As shown in figure 1.2

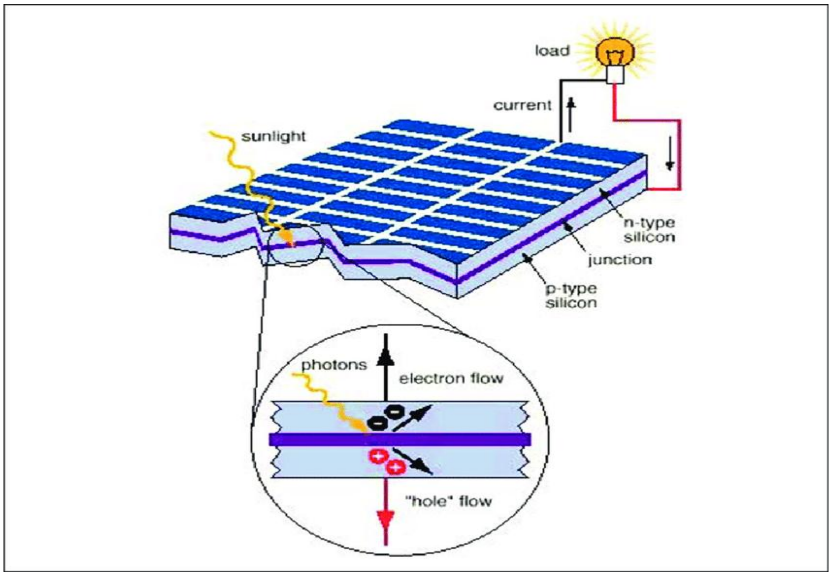

Figure 2: General structure of a photovoltaic panel [4]

1.3 Components of a Photovoltaic System

A complete photovoltaic system includes several main components:
PV Modules or Panels: These are the core units that capture sunlight and convert it into DC electricity.
Inverters: These convert DC output from the panels into alternating current (AC), which is suitable for use by common electrical equipment or for grid connection.
Mounting Structures: These hold the panels in place at the correct angle to collect sunlight.
Electrical Protection Devices: Fuses and surge protectors keep the system safe.
Optional Batteries: In off-grid systems, batteries store energy for use when sunlight is not available.

1.4 Advantages and Limitations of Photovoltaic Systems

Photovoltaic systems offer several advantages. They produce clean electricity without direct emissions or fuel costs. Once installed, operating costs are low compared with conventional power plants. However, PV systems also have limitations. The power output depends on solar irradiance and weather conditions. Performance can decrease because of temperature changes and other environmental factors.

1.5 Soiling and Environmental Impacts

In real outdoor conditions, environmental factors such as dust, sand, and pollution affect the performance of solar panels. The accumulation of dust and dirt on panel surfaces, known as soiling, reduces the amount of sunlight that reaches the cells. Research shows that soiling can significantly reduce energy output if not cleaned regularly.

This issue is especially important in arid and semi-arid regions where dust deposition rates are high. Therefore, cleaning and maintenance become essential to maintain performance and extend the lifetime of photovoltaic systems. As shown in figures 1.5.1 and 1.5.2

Figure 3: Soiling accumulation on a solar panel surface [5]

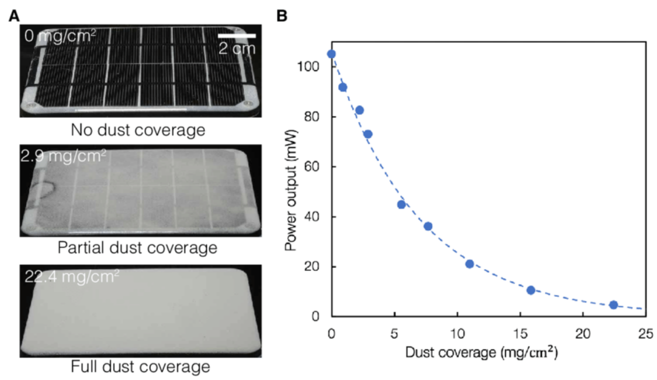

Figure 4: Power loss from soiling [5]

The electrical behavior of a photovoltaic module is described by its current voltage (I–V) and power voltage (P–V) characteristics. These curves are derived from the equivalent electrical model of the solar cell and are essential for understanding module performance under different environmental conditions.

1.6 Single Diode Model of a PV Cell

A photovoltaic cell can be represented by the single diode model, which includes a current source, a diode, a series resistance Rs, and a shunt resistance Rsh.

The current output I of the cell is given by:

$I = I_{ph} - I_o \left[\exp\left((V + I R_s) / (n V_t)\right) - 1 \right] - (V + I R_s) / R_{sh}$. (1.1)

Where:

I_{ph} is the photocurrent

I_o is the diode saturation current

V is the output voltage

n is the diode ideality factor

V_t is the thermal voltage

R_s is the series resistance

R_{sh} is the shunt resistance

This model is widely used in photovoltaic analysis and is discussed in publications from the National Renewable Energy Laboratory and in scientific journals such as Renewable and Sustainable Energy Reviews.

1.6.1 I-V Characteristic Curve

The I V curve represents the relationship between current and voltage for a given irradiance and temperature.

Two important operating points are defined:
Short circuit condition:
$V = 0$ and $I = I_{sc}$ (1.2)
When you connect the positive and negative terminals together, voltage drops to zero. With no voltage, the current flowing is purely what the sunlight generates this is the maximum current the cell can produce, called Isc.

Open circuit condition:
$I = 0$ and $V = V_{oc}$ (1.3)
When you leave the terminals disconnected, no current flows. The voltage builds up inside the cell until it balances the photocurrent. This maximum voltage with zero current is called Voc.

Between these two points, the curve shows a nonlinear behavior. The shape of the curve is influenced by internal resistance and environmental conditions.
The fill factor FF is defined as:
$FF = (V_{mp} \times I_{mp}) / (V_{oc} \times I_{sc})$ (1.4)
The fill factor tells you how "square" the I-V curve is. It compares the actual best power the cell delivers against the ideal power it would deliver if it could output Isc and Voc at the same time. A higher number means a better cell with less internal loss.

It represents the quality of the photovoltaic module and directly affects efficiency, As shown in figure 1.6.1

1.6.2 P-V Characteristic Curve and Maximum Power Point

The output power is calculated as:

$P = V \times I$ (1.5)

The P V curve presents a single maximum point known as the Maximum Power Point MPP. This point corresponds to the optimal operating condition of the module.

At this point:

$P_{max} = V_{mp} \times I_{mp}$ (1.6)
The maximum power point is where the product of voltage and current is highest. This is the sweet spot between too little voltage and too little current. Practical systems use MPPT controllers to stay at this point.

In practical systems, Maximum Power Point Tracking algorithms are implemented in the inverter to maintain operation near this point under varying environmental conditions, As shown in Figure 5

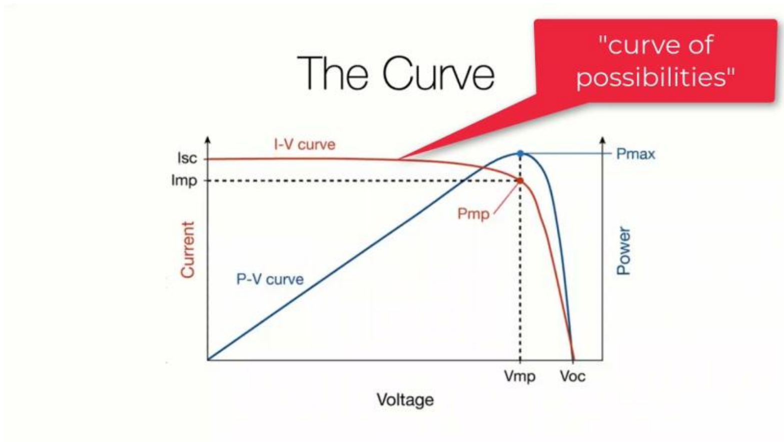

Figure 5: Maximum power point characteristics for I–V and P–V curves [6]

1.6.3 Effect of Solar Irradiance

Solar irradiance directly affects the photocurrent Iph. An increase in irradiance results in an almost proportional increase in short circuit current Isc.
The open circuit voltage Voc increases slightly with irradiance due to its logarithmic dependence on photocurrent.
Experimental studies [7] published in Renewable and Sustainable Energy Reviews confirm that irradiance variation is the primary factor influencing daily and seasonal energy production, illustrated in figure 1.6.2

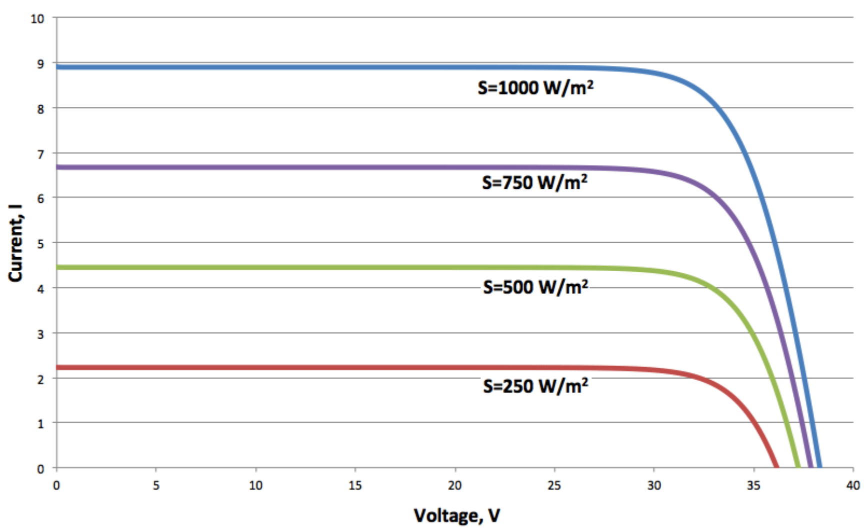

Figure 6: Energy production based on irradiance variation [8]

1.6.4 Effect of Temperature

Temperature mainly affects the open circuit voltage. As temperature increases, the diode saturation current Io increases, which leads to a reduction in Voc.

The temperature coefficient of voltage is typically negative, meaning that power output decreases with increasing temperature.

High temperature operation is common in arid climates. According to reports from the International Energy Agency, temperature related losses are significant in desert regions.

This aspect is particularly important for this study because elevated temperatures also accelerate inverter component aging and increase maintenance requirements, illustrated in Figure 7

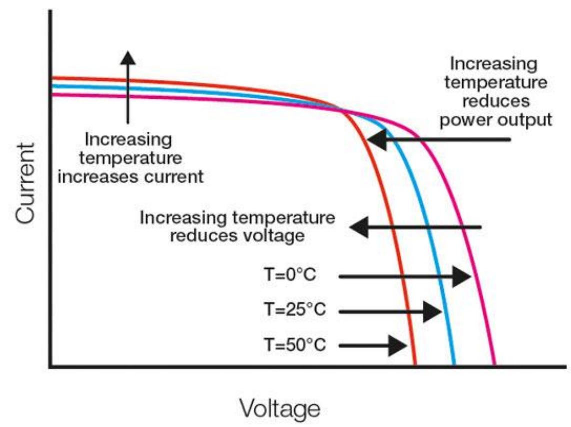

Figure 7: Effect of temperature on voltage and current [8]

1.7 Maximum Power Point

The Maximum Power Point is the operating condition at which the photovoltaic module produces its highest power output for given environmental conditions. It corresponds to a specific voltage and current combination on the I V curve.

In practical systems, Maximum Power Point Tracking controllers are used in inverters to continuously adjust the operating voltage and maintain operation near the MPP.

Understanding the Maximum Power Point is important because any deviation from this point results in reduced energy production. Environmental factors such as dust accumulation and high temperature can shift the MPP and reduce overall system efficiency. As shown in figure 1.7

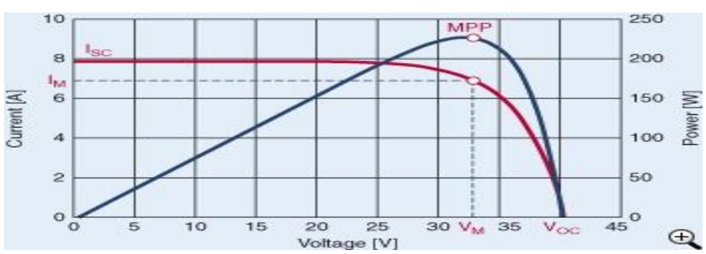

Figure 8: Maximum power point on the P–V curve [9]

Conclusion

This chapter presented the fundamental principles of photovoltaic solar energy systems. Solar energy was introduced as a clean, abundant renewable resource, with photovoltaic technology offering a direct conversion pathway from sunlight to electricity through the photovoltaic effect in semiconductor materials. The components of a complete PV system—modules, inverters, mounting structures, and protection devices—were described, alongside the advantages and limitations of such installations.

The single diode model was presented as the standard electrical representation of a PV cell, with the I-V and P-V characteristic curves illustrating key operating parameters including short-circuit current, open-circuit voltage, fill factor, and the Maximum Power Point. Environmental effects were analyzed: solar irradiance directly determines photocurrent and dominates energy production variation, while temperature inversely affects open-circuit voltage and overall efficiency—a critical concern for arid climates. Soiling was identified as a major operational challenge, with dust accumulation significantly reducing light transmission and energy output. Understanding these electrical characteristics and environmental dependencies establishes the technical foundation for evaluating maintenance strategies and the need for effective cleaning solutions in subsequent chapters.

CHAPTER 2

Maintenance Challenges of Photovoltaic Systems in Arid Environments

2.1 Environmental Conditions in Arid Regions

Arid and semi-arid regions are characterized by high solar irradiance, making them highly suitable for photovoltaic energy production. According to the International Energy Agency, these regions offer strong potential for large-scale solar installations.

However, these environments also present several challenges. High temperatures reduce photovoltaic efficiency by decreasing the open circuit voltage, which leads to lower power output. In addition, dust storms and airborne particles are common, causing continuous accumulation of dust on panel surfaces. Due to low rainfall, natural cleaning is very limited, allowing dust to build up over time.

Wind contributes to dust transport and can lead to uneven deposition on panels, which may cause localized shading. Furthermore, water scarcity makes traditional cleaning methods difficult and costly to implement.

These conditions result in continuous performance degradation, making regular and efficient maintenance essential, especially in arid climates.

Figure 9: A solar panel farm in an arid environment [10]

2.2 Dust Deposition and Soiling Mechanisms

Dust accumulation on photovoltaic modules, commonly referred to as soiling, is one of the main factors affecting system performance in arid and semi-arid regions. Airborne particles such as sand, soil, and pollutants are transported by wind and gradually settle on the surface of solar panels.

The deposition of dust is influenced by several mechanisms, including gravity, wind velocity, electrostatic forces, and surface properties of the panel. In dry environments, the absence of rainfall prevents natural cleaning, allowing dust layers to build up over time. This accumulation becomes more significant with prolonged exposure and lack of maintenance.

Dust particles adhere to the panel surface, forming a layer that reduces light transmission. of solar radiation to the photovoltaic cells. As a result, the amount of absorbed light decreases, leading to a reduction in the generated current and overall power output.

In addition, dust deposition is often non-uniform, especially under variable wind conditions. This uneven distribution can cause partial shading of the cells, which leads to mismatch losses within the module. Over time, this effect can contribute to localized overheating and further degradation of the system.

Studies [11] reported in Results in Engineering confirm that soiling losses can become significant if cleaning is not performed regularly, particularly in desert environments.

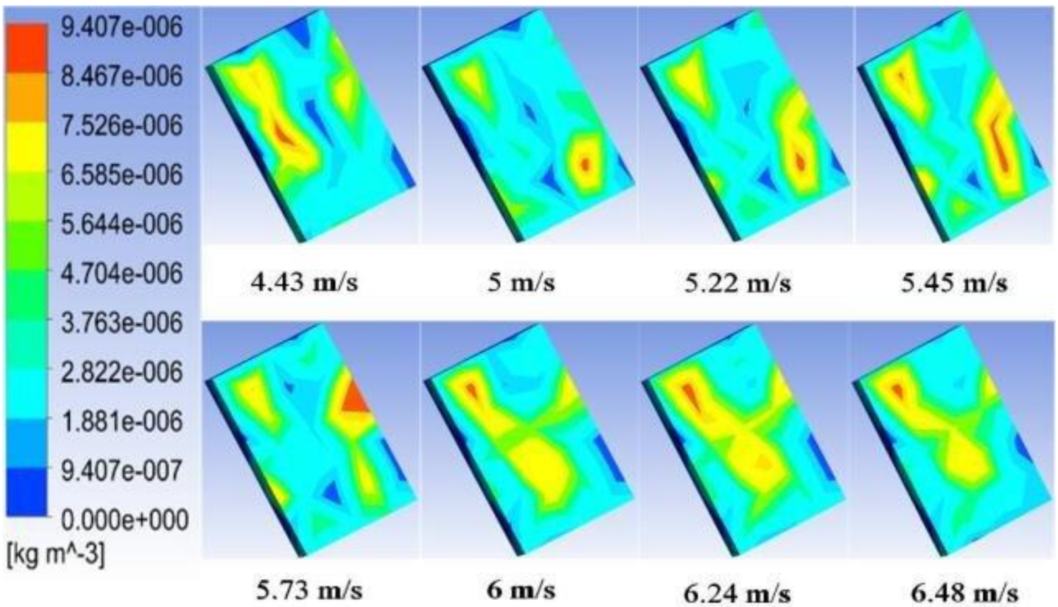

Figure 10: Diagram of dust deposition on the PV panel [12]

The rate of dust accumulation depends on environmental factors such as wind speed, particle size, and exposure duration.

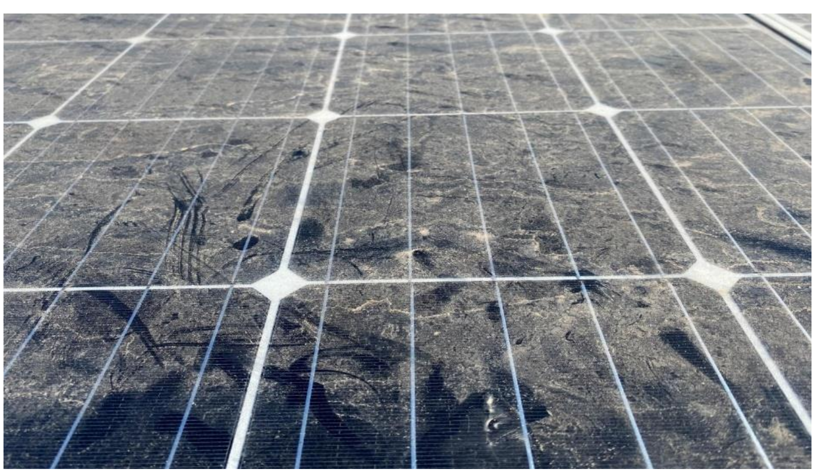

Figure 11: Non-uniform dust distribution on solar panels [13]

2.3 Impact of Soiling on Electrical Performance

Dust accumulation on photovoltaic modules has a direct impact on their electrical performance. The presence of a dust layer reduces the amount of solar radiation reaching the cells, which leads to a decrease in the generated photocurrent. As a result, the short circuit current (Isc) is significantly reduced.

The open-circuit voltage (Voc) is less affected by soiling, as it depends logarithmically on the current. However, the overall power output of the module decreases due to the combined reduction in current and operating efficiency.

Soiling also affects the shape of the I–V and P–V curves. The maximum power point (MPP) shifts to lower values, resulting in reduced energy production. This effect becomes more pronounced as dust accumulation increases over time.
In some studies [14], power losses due to soiling can reach between 20% and 50% in desert environments without regular cleaning.

In addition, non-uniform dust deposition can cause partial shading of certain cells within the module. This leads to mismatch losses, where some cells operate at different current levels than others. In severe cases, this can result in hotspot formation, which increases the risk of long-term damage to the module.

Studies reported in Renewable and Sustainable Energy Reviews show that soiling can cause significant energy losses [15], especially in arid environments where cleaning is not performed regularly.

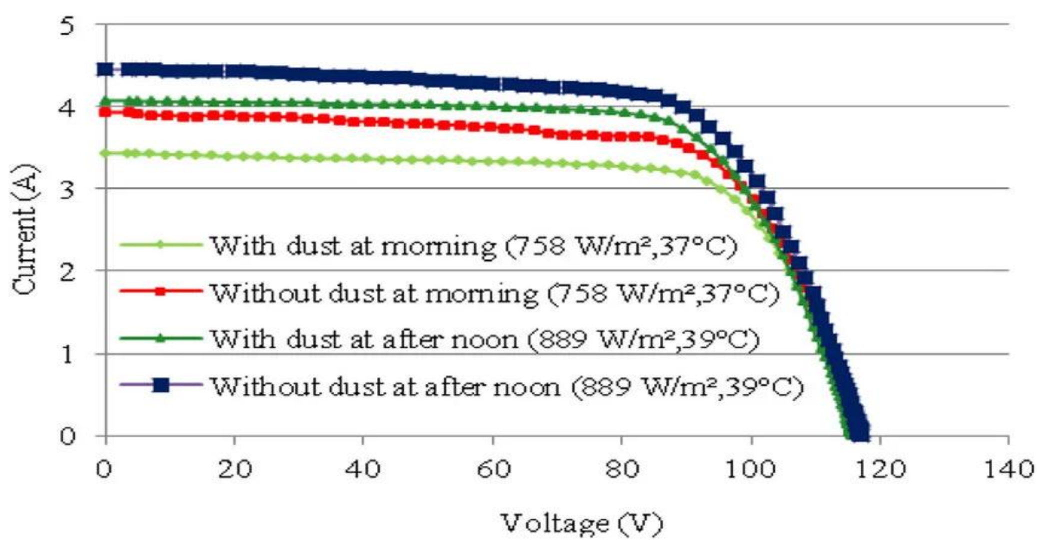

Figure 12: Power loss due to soiling across the day [16]

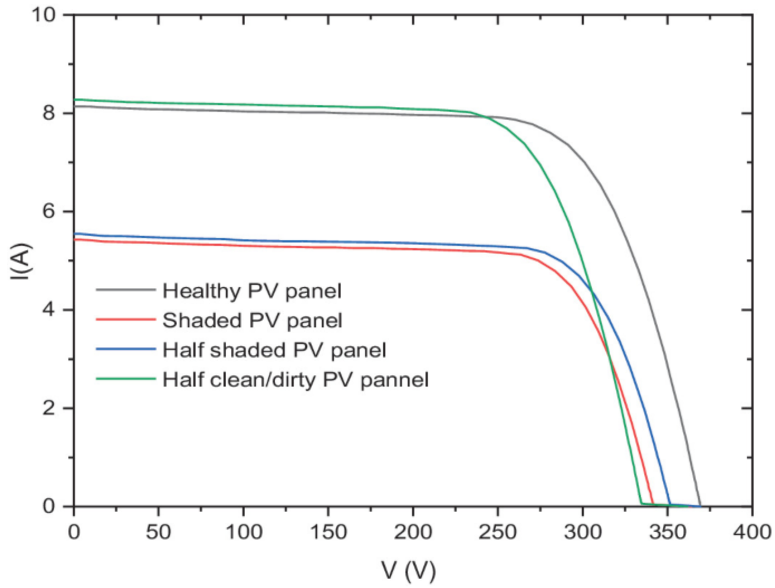

Figure 13: Impact of dust accumulation and partial shading on solar panels [17]

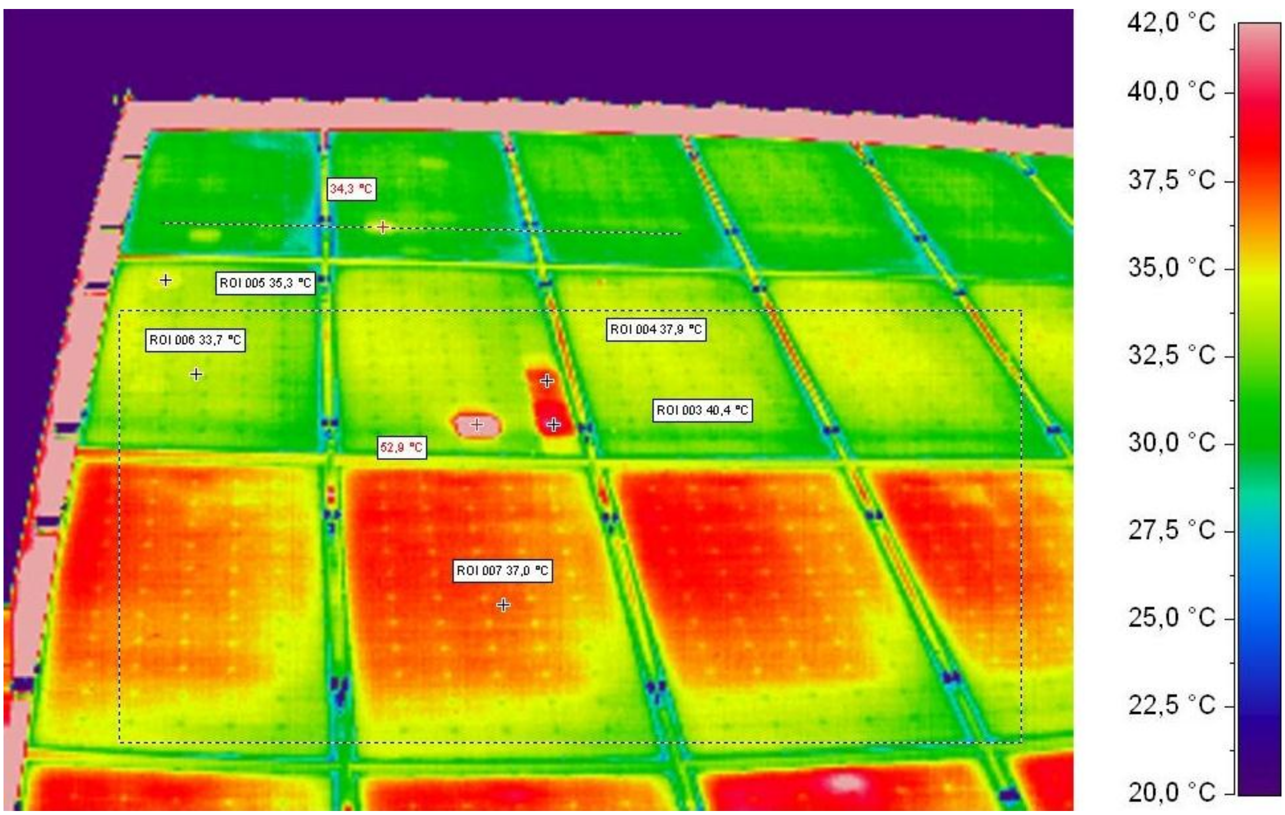

Figure 14: Hot spots on solar panels caused by soiling [18]

2.4 Existing Cleaning Methods and Limitations

Photovoltaic modules require regular cleaning to maintain their performance, especially in arid environments where dust accumulation is significant. Several cleaning methods are currently used in practice, each with its advantages and limitations.

Manual cleaning is the most common method. It involves workers using water, brushes, or cloths to remove dust from the panel surface. While this method is simple and effective for small installations, it becomes impractical for large-scale solar plants. It also involves high labor costs and potential safety risks, particularly when panels are installed at height.

Water-based cleaning systems are widely used due to their effectiveness in removing dust. However, in arid regions, water is a scarce resource, making this method costly and sometimes unsustainable. Frequent use of water can also lead to mineral deposits on the panel surface if not properly managed.

Mechanical cleaning systems, such as fixed brushes or automated rails, have been developed to reduce manual effort. These systems can operate regularly and improve cleaning consistency. However, they often require complex installation, regular maintenance, and may not adapt well to different panel configurations.

Despite these solutions, several limitations remain. High water consumption, operational cost, system complexity, and limited adaptability reduce the overall efficiency of existing cleaning methods. In addition, many systems are not fully autonomous and still require human intervention.

These limitations highlight the need for an automated, efficient, and low-resource cleaning solution, particularly for large-scale photovoltaic installations in arid regions.

Figure 15: Manual solar panel cleaning workers [19]

Figure 16: Existing commercial solar panel cleaning robot system [20][23]

2.5 Preventive Maintenance of Photovoltaic Systems

In addition to cleaning, photovoltaic systems require regular preventive maintenance to ensure long-term reliability and performance. Maintenance operations include inspection of electrical connections, monitoring of system performance, and periodic replacement of critical components.

One of the most important components is the inverter, which converts direct current into alternating current. According to the National Renewable Energy Laboratory, inverter failures are among the most common causes of system downtime. This is mainly due to the aging of internal components such as electrolytic capacitors, especially under high temperature conditions.

Regular inspection of wiring and connections is also necessary to prevent energy losses and ensure system safety. Loose or degraded connections can lead to increased resistance, overheating, and reduced efficiency.

Preventive maintenance strategies help reduce unexpected failures, extend system lifetime, and maintain stable energy production

Conclusion

This chapter examined the specific degradation mechanisms affecting photovoltaic installations in arid and semi-arid regions. Environmental conditions characteristic of these climates—high solar irradiance, elevated temperatures, frequent dust storms, low rainfall, and water scarcity—create a challenging operational context where natural cleaning is minimal and performance degradation is accelerated.

The mechanisms of dust deposition and soiling were analyzed, including gravity settling, wind-driven transport, electrostatic adhesion, and the formation of non-uniform dust layers leading to partial shading. The electrical consequences were quantified: soiling reduces photocurrent and shifts the Maximum Power Point downward, with power losses reaching 20–50% in desert environments without regular maintenance. Non-uniform soiling further introduces mismatch losses and hotspot formation risks, threatening long-term module integrity.

Existing cleaning methods were reviewed and their limitations identified: manual cleaning is labor-intensive and unsafe for large installations; water-based methods are unsustainable in water-scarce regions; and mechanical systems often suffer from high cost, complex installation, and poor adaptability. Preventive maintenance beyond cleaning—particularly inverter component monitoring—was highlighted as essential for system reliability. These challenges collectively motivated the need for an automated, water-efficient, low-cost robotic cleaning solution, which is presented in the following chapter.

CHAPTER 3

Design and Development of the Robotic Cleaning System

3.1 General Description of the Proposed System

The proposed robotic cleaning system is an automated device designed to traverse photovoltaic panel arrays in arid and semi-arid environments and restore their energy output by removing accumulated dust and soiling. The robot is built around a single cylindrical brush that rotates against the panel surface while water is sprayed ahead of it through six nozzles, followed by two squeegee blades that remove excess water from either direction of travel. The robot moves horizontally across the full length of a panel series in one continuous pass. The standard cleaning cycle described in this work is evaluated for a 20-meter panel row, representing a typical commercial installation. The robot is capable of cleaning significantly longer series as long as external power and water supply are maintained.

The system is powered by an external 12-volt electrical supply to ensure consistent operation regardless of solar conditions. This eliminates the need for onboard batteries and their associated weight, cost, and charging complexity. The robot is activated through a remote controller or a smartphone application via wireless connection. There is no physical start button on the robot body, keeping the exterior sealed against dust and moisture.

A defining feature of the design is its wheel arrangement and clamping mechanism. The robot uses eight wheels in total, four on each side. On each side, two wheels ride on the bottom surface of the aluminum panel frame and two wheels ride on the top surface of the same frame. The panel frame is therefore gripped between upper and lower wheels like a train on rails. Compression springs push the top wheels downward, generating the clamping force that holds the robot securely during translation. This passive mechanical system allows the robot to adapt to different frame thicknesses automatically.

The robot has an adjustable effective cleaning width. The standard brush length is approximately one meter, matching typical commercial panels. For wider panels, a longer brush is employed.

The water used for cleaning is supplied either from an external storage tank or, in an alternative configuration, reused from the photovoltaic panels' own cooling system.

A pumping system delivers water through two main pipes connected to a distribution manifold, which evenly supplies six spray nozzles positioned in front of the cleaning brush. This arrangement ensures uniform water distribution across the panel surface prior to brushing and squeegee drying.

Edge detection is performed using two waterproof ultrasonic distance sensors (A02YYUW), mounted symmetrically on both sides at the front of the robot. These sensors continuously measure the distance to the panel edge, enabling the system to detect boundaries and prevent the robot from moving outside the photovoltaic surface. Figure 17 shows the structure

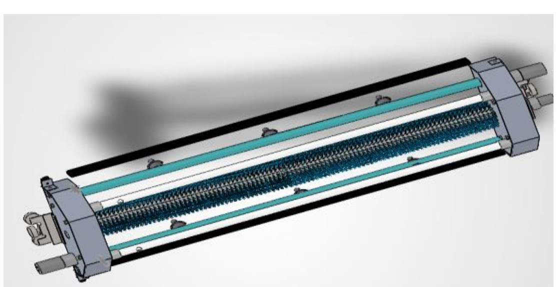

Figure 17: Overall 3D model of the proposed robotic cleaning system (own design)

Interpretation: The isometric view shows the robot's overall layout — the two side rails carrying the spring-loaded clamping wheels, the central cylindrical brush and spray bar, and the trailing squeegee — all mounted on the lightweight aluminum frame described in Section 3.1.

3.1.1 Adaptability to Non-Standard Panel Widths

The base configuration of the robotic cleaning system is designed with a brush length of approximately one meter, matching the standard width of commercial photovoltaic panels. For installations with wider panels, the system employs a modular brush architecture: the cylindrical brush is mounted on a splined shaft with quick-release couplings, allowing the operator to replace it with a longer brush (1.5 m or 2.0 m) without tools. The water manifold, squeegee rails, and frame cross-members are sized to accommodate the maximum brush length.

This approach was chosen over a serpentine repositioning mechanism because:

- It eliminates a motorized actuator, reducing cost, mass, and failure modes
- It avoids the 16–17 second repositioning delay between passes
- It maintains continuous autonomous operation without operator intervention during the cleaning cycle
- Brush replacement requires less than 60 seconds and is performed once per installation type

The water nozzles don't need a change simply allowing them to use more water and installing longer squeegee blades is enough to clean a non-standard panel.

3.2 Mechanical Design of the System

The mechanical structure was designed using SolidWorks with emphasis on simplicity, durability, and low manufacturing cost. The design eliminates unnecessary complexity by using a single cylindrical brush, a passive spring-clamping wheel system, and standard components available from general industrial suppliers

3.2.1 Robot Base Structure

The main frame is a rigid rectangular structure fabricated from aluminum alloy extrusion It spans approximately one meter in length in the standard configuration, with adaptability to larger panels via changing the brush to favor a longer one described in Section 3.1.1, and its height is approximately 150 to 200 millimeters to accommodate the wheel diameter, brush assembly, The frame consists of two parallel longitudinal members connected by cross braces. The longitudinal members contain the guides for the spring-loaded wheel carriages, mounting points for the fixed wheel shafts, and channels for routing cables and water tubing internally. All joints use standard metric fasteners. The design avoids welded joints or custom machining to minimize manufacturing cost and allow assembly with hand tools as shown in Figure 18.

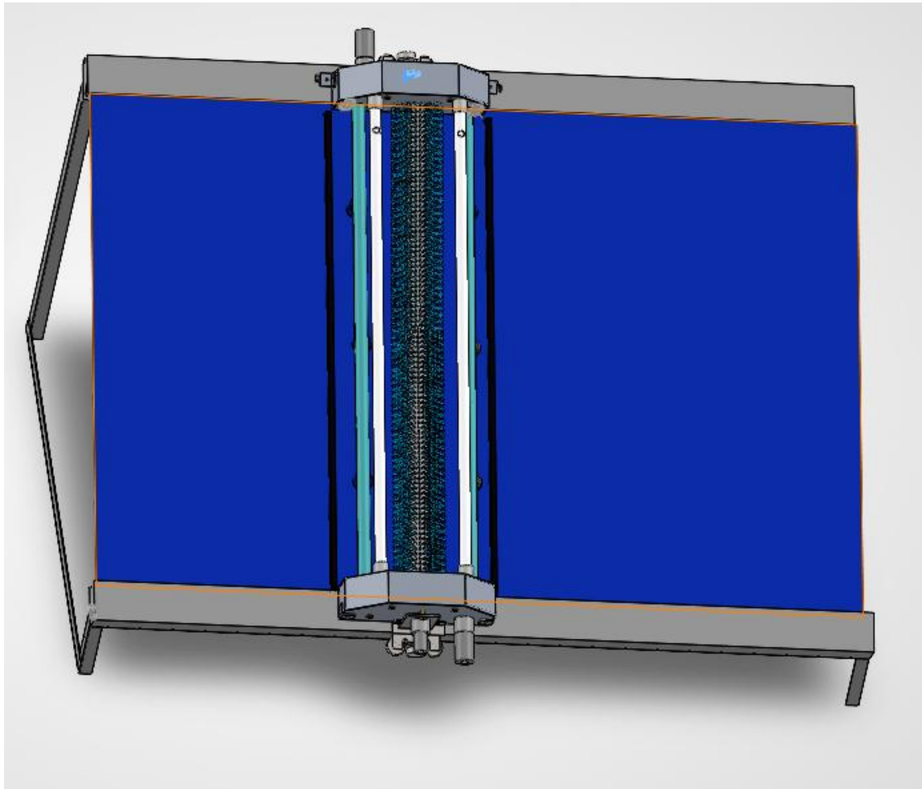

Figure 18: Robot base frame and structural assembly (own design)

Interpretation: The two parallel longitudinal members and cross braces form the load-bearing skeleton of the robot; the channels along the rails route the wheel-carriage guides, internal cabling, and water tubing described in the surrounding text.

3.2.2 Wheel System and Clamping Mechanism

The robot employs eight wheels arranged as four per side. On each side, two wheels contact the bottom surface of the aluminum panel frame, and two wheels contact the top surface of the same frame. This creates a clamping action where the frame is gripped between upper and lower wheels, preventing the robot from lifting off or tipping while allowing smooth linear translation along the panel edge.

The bottom wheels on each side are the drive wheels. Each pair of bottom wheels is driven by a single DC motor through a common shaft or short belt drive. Using one motor per side rather than one motor per wheel reduces cost and complexity. The wheel material is hard polyurethane, chosen to provide adequate traction on aluminum without leaving residue or causing abrasive wear. Wheel diameter is 40 millimeters and width is 15 millimeters. The wheels use sealed ball bearings to exclude dust and moisture.

The top wheels on each side are idler wheels. They are not motorized. Their function is to press downward against the top surface of the aluminum frame, working with the springs to generate normal force for traction. These wheels also use sealed ball bearings and are mounted on stationary axles attached to sliding carriages.

The clamping force is generated by four compression springs, two per side. Each spring is positioned between the upper frame member and the sliding carriage that carries the top wheels. The springs push the carriage downward, pressing the top wheels against the frame and thereby forcing the bottom wheels upward against the frame underside. A total clamping force of approximately 25 newtons per side is typical. The springs are stainless steel cylindrical compression springs with guided mandrels to prevent buckling. Mechanical stops limit maximum extension to prevent spring release during installation.

This spring system allows passive adaptation to different frame thicknesses. When installed on a thicker frame, the springs compress further and generate higher force. When installed on a thinner frame, the springs extend and generate lower force. Standard photovoltaic panel frames range from 30 to 50 millimeters in thickness, and the spring rate is chosen to maintain adequate clamping force across this range, see Figure 19 below.

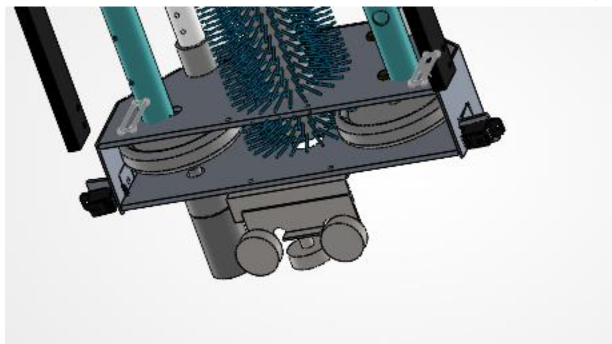

Figure 19: Clamping wheel arrangement used for panel attachment (own design)

Interpretation: Each wheel carriage rides on a captive compression spring so that it can slide outward and press against the panel frame, keeping the robot clamped to the glass as it moves; this arrangement accommodates the 30 to 50 millimeter frame-thickness range discussed above.

3.2.3 Drive Motors and Torque Analysis

Two DC motors provide propulsion, one for each side. Each motor drives the two bottom wheels on its side. The motors are 12-volt brushed DC units with integrated gearboxes providing a reduction ratio of approximately 15 to 1. This reduces the motor output from 300 revolutions per minute to approximately 20 revolutions per minute at the wheel, corresponding to a translation speed of approximately 4.2 centimeters per second with 40-millimeter wheels.

The motor torque requirement is determined by the total resistance force opposing motion. This resistance has five components. The gravity component acts along the inclined panel surface and equals the robot mass multiplied by the gravitational acceleration and the sine of the panel tilt angle θ: $F\_gravity(\theta) = m \cdot g \cdot \sin(\theta)$. This formulation is left as a function of θ, rather than fixed at a single value, so that the sizing applies to any panel tilt encountered across arid and semi-arid installations, where mounting angles are generally chosen close to the site latitude and typically fall in the range of roughly 10° to 35°. For a robot mass of 3 kilograms, this gives F_gravity(10°) ≈ 5.11 N, F_gravity(20°) ≈ 10.07 N, F_gravity(25°) ≈ 12.40 N, F_gravity(30°) ≈ 14.72 N, and F_gravity(35°) ≈ 16.88 N. The mid-range value of 25° is used below as a representative worked example, with the full range checked afterward. Rolling resistance arises from the deformation of the polyurethane wheels against the aluminum frame and is calculated using a rolling resistance coefficient of 0.008 multiplied by the total normal force on all wheels. The total normal force includes both the weight component perpendicular to the panel and the clamping force from the springs, giving 76.67 newtons total normal and 0.61 newtons rolling resistance. Brush drag results from the bristle engagement with the glass surface and is estimated at 0.80 newtons for the 1-meter-wide brush with 2 millimeters penetration. Squeegee drag from the two silicone blades with 3 millimeters compression is 1.50 newtons. Bearing friction from all 16 wheel bearings contribute an equivalent force of 0.80 newtons.

At the representative 25° tilt, the sum of all resistance forces is 16.11 newtons. With two motors sharing the load equally, each motor must overcome 8.06 newtons. At the 20-millimeter wheel radius and through the 15-to-1 gear reduction with 85 percent efficiency, the required torque at each motor shaft is 12.64 millinewton-meters. The selected motors have a stall torque of 200 millinewton-meters, providing a safety factor of approximately 16 relative to the nominal load at this tilt. Because the gravity term is the only tilt-dependent component, the same method applies directly at any other tilt angle by substituting $\sin(\theta)$: the total resistance is $R(\theta) = 3.71\text{ N} + 3 \cdot 9.81 \cdot \sin(\theta)$, giving $R(10°) \approx 8.82$ N, $R(20°) \approx 13.78$ N, $R(25°) \approx 16.11$ N, $R(30°) \approx 18.43$ N, and $R(35°) \approx 20.59$ N — covering the full range of tilt angles used across arid and semi-arid solar farms. Even under worst-case conditions, combining the steepest tilt in this range (35°) with double the normal brush drag, the required torque increases to approximately 17.3 millinewton-meters per motor, still yielding a safety factor of about 11.5. The design therefore retains a comfortable torque margin at any tilt angle representative of arid or semi-arid photovoltaic installations, not only the 25° case used as the worked example.

Traction is verified by comparing available friction to required force. With a friction coefficient of 0.4 between polyurethane and aluminum and a clamping force of 25 newtons per side, the total available traction is 30.67 newtons, independent of tilt angle since it depends only on the clamping force. Since the total resistance is 16.11 newtons at the representative 25° tilt, the traction margin is 1.90. Even at the steepest tilt considered (35°), where resistance rises to 20.59 newtons, the traction margin remains 1.49, confirming that the wheels will not slip under normal operating conditions across the full range of tilt angles used in arid and semi-arid installations.

Figure 20: Drive motor and wheel assembly (own design)

Interpretation: The planetary-gearbox motor is coupled directly to the wheel shaft on one side of the robot; an identical unit on the opposite rail provides independent, symmetric propulsion.

3.2.4 Cylindrical Brush and Cleaning Mechanism

The cleaning element is a single cylindrical brush mounted transversely across the robot body. The cylinder is approximately 1 meter long in the standard configuration and 80 millimeters in diameter, covered with nylon bristles of medium stiffness. Bristle length is 25 millimeters with a density of approximately 500 bristles per square centimeter. This configuration provides effective dust dislodgment without scratching the tempered glass surface of the photovoltaic panel.

The brush is driven by a dedicated 12-volt DC motor mounted at one end of the cylinder. The motor has a stall torque of 100 to 150 millinewton-meters and drives the brush at 60 to 120 revolutions per minute through a flexible coupling. This corresponds to a bristle tip surface speed of 0.25 to 0.50 meters per second, sufficient to lift dust particles without generating excessive heat or static charge. The brush shaft is supported by two ball bearings mounted on adjustable brackets that allow fine-tuning of bristle penetration depth during installation.

Ahead of the brush, six brass mist nozzles are arranged in a line across the panel width. The nozzles have an orifice diameter of 0.3 millimeters and produce a fine conical spray pattern. Water is supplied to the nozzles through two polyurethane pipes running from a distribution manifold. The use of two pipes rather than one provides redundancy and allows uniform flow distribution across the full width. The total flow rate from all six nozzles is approximately 0.5 liters per minute at the operating pressure.

Water for the system is supplied externally from a tank, reused solar-panel cooling water, or a direct water line. When an external tank is used, a separate 12-volt diaphragm pump pressurizes the water and delivers it to the robot via a supply hose. In the direct water line configuration, no pump is needed.

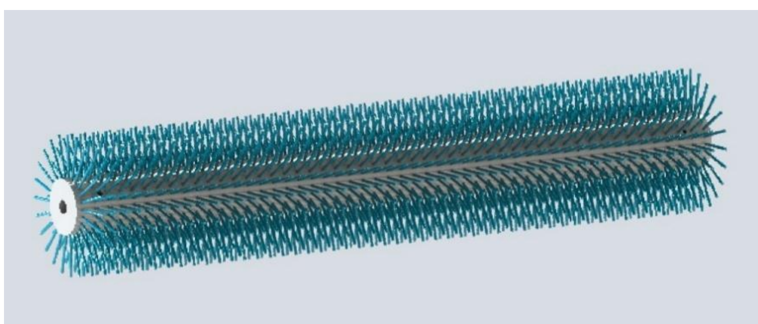

Figure 21: Cylindrical brush and spray-nozzle assembly (own design)

Interpretation: The cylindrical brush is flanked by spray nozzles that wet the panel surface immediately ahead of the bristles, loosening dust before it is swept away.

3.2.5 Edge Detection and Safety System

Two waterproof ultrasonic distance sensors (A02YYUW) are mounted on the robot, one on each side at the leading end. These sensors measure distance using ultrasonic sound waves rather than light, providing accurate detection independent of surface color, reflectance, or ambient light. Each sensor has a measurement range of 3 to 450 centimeters with millimeter-level resolution and a 60-degree field of view. They operate on 3.3 to 5 volts and communicate via I2C protocol.

During operation, the sensor on the direction of travel continuously measures the distance to the panel surface ahead. When the robot approaches the end of the panel row, the surface terminates and the measured distance increases sharply. The control system detects this transition and initiates the stop sequence, de-energizing all motors and the pump. The dual sensor arrangement provides redundancy in case one sensor becomes obscured by dust or water spray, as shown in figure 3.5.

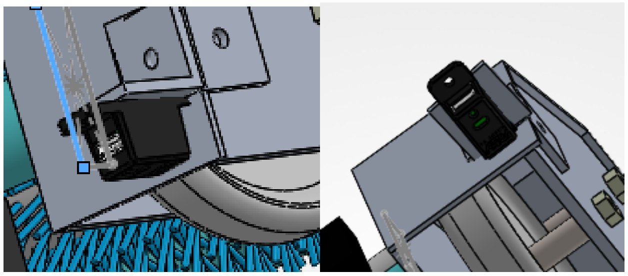

Figure 22: Mounting position of the edge-detection sensors (own design)

Interpretation: The two time-of-flight sensors are mounted at the leading corners of the robot, angled slightly outward so that each one detects the panel edge on its own side before the robot travels past it.

3.2.6 Squeegee system

The squeegee blades are fabricated from silicone rubber with a continuous T-slot groove running along the top edge. The robot body features protruding rails on each side that match this groove. The blade is installed by sliding the groove onto the rail, which locks it in place along the full width. The silicone material provides natural compliance — it flexes to follow minor surface undulations and maintains uniform wiping pressure without additional springs or mechanisms. To replace or adjust the blade, it simply slides off the rail.

3.3 Control and Communication System

The control system is built around a single ESP32 microcontroller module. This platform was selected because it integrates a dual-core processor with built-in Wi-Fi and Bluetooth connectivity on one chip, providing wireless connectivity for the remote control and smartphone application, sufficient processing power for the energy-based AutoStart algorithm, and multiple GPIO pins for sensor and motor interfaces.

Two BTS7960 43 A half-bridge motor drivers control the drive motors, providing direction reversal and pulse-width modulation speed control. A single-channel driver controls the brush motor. The water solenoid valve is switched through a relay to control flow into the robot. If an external pump is used, it may be activated simultaneously or run independently depending on the installation configuration.

The wireless interface allows an operator to initiate cleaning cycles remotely and receive status updates. The automatic start capability monitors photovoltaic array output through a voltage and current sensing circuit. When measured power falls below a predetermined threshold of expected power, indicating soiling, the control system triggers a cleaning cycle automatically.

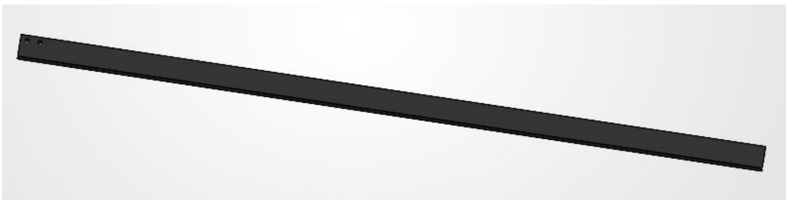

3.4 Water Supply Configurations

The robotic cleaning system does not carry an onboard water tank. Instead, water is supplied entirely from external sources, which reduces the robot's weight, simplifies its mechanical structure, and eliminates the need for periodic refilling during operation.

Three external water source configurations are supported:

3.4.1 External Storage Tank

A separate water tank is positioned near the photovoltaic installation. A 12-volt diaphragm pump draws water from this tank through an inlet filter and pressurizes it for delivery to the robot via a flexible supply hose. The pump is activated by the robot's control system at the start of each cleaning cycle. The tank capacity is sized according to the number of panels and cleaning frequency; a typical 50-liter tank is sufficient for multiple cleaning cycles before refilling.

Figure 23: External water storage tank configuration (own compilation)

Interpretation: The tank sits beside the panel array and feeds the robot through the diaphragm pump and inline mesh filter described in Section 3.4.1.

3.4.2 Solar-Panel Cooling System Water Reuse

As an alternative or supplemental source, water already available on site from a photovoltaic cooling system can be reused for cleaning. Active PV cooling installations spray or circulate water across the back or front of the panels to reduce cell temperature and recover the efficiency lost to heat, and this water is typically collected in a drainage channel or sump beneath the array rather than being discarded. A small transfer pump routes this recovered cooling water to the robot’s external supply tank (Section 3.4.1) through the same inline mesh filter used for the other supply configurations. Because the water has already been used once for cooling, this configuration adds essentially no extra water demand to the site and is particularly attractive for installations that already operate a cooling system, which is increasingly common on large arid and semi-arid solar farms.

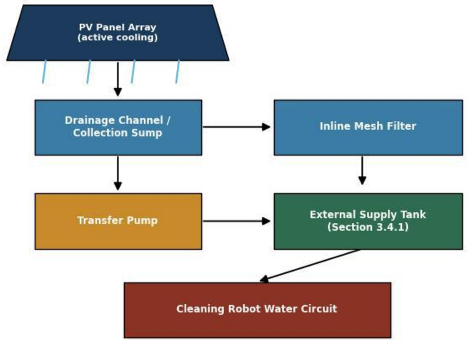

Water reuse from the solar-panel cooling system

3.4.3 Direct Water Line Connection

For installations with access to a pressurized water supply, the robot can connect directly to a standard water pipe through a pressure regulator and particulate filter. This configuration eliminates the need for any tank or pump (other than the supply line's existing pressure), further reducing system complexity and ensuring unlimited water availability.

Figure 24: Direct connection to a pressurized water line (own compilation)

Interpretation: A pressure regulator and particulate filter connect the robot’s supply hose directly to an existing water line, removing the need for a tank or pump at the array.

3.4.4 Water Distribution on the Robot

Regardless of the source, water reaches the robot through a single supply hose connected at the robot's rear via a quick-disconnect fitting. Inside the robot, water flows through two polyurethane distribution pipes to a manifold, which evenly supplies six brass mist nozzles positioned ahead of the cleaning brush. The nozzles have an orifice diameter of 0.3 mm and produce a fine conical spray pattern. The total flow rate is approximately 0.5 liters per minute at operating pressure.

A small 12-volt solenoid valve on the robot controls water flow, opening only during active cleaning to prevent dripping and conserve water. A mesh filter at the hose inlet protects the nozzles from clogging due to dust or debris.

3.5 Impact of Maintenance on Photovoltaic Performance

Maintenance plays a critical role in ensuring the efficiency and long-term performance of photovoltaic systems. In arid and semi-arid regions, dust accumulation significantly reduces the amount of solar radiation reaching the panel surface, leading to a decrease in energy production.

Several studies reported in Renewable and Sustainable Energy Reviews [14] indicate that power losses due to soiling can reach between 20% and 50% if panels are not cleaned regularly. These losses increase over time as dust continues to accumulate, especially in environments with low rainfall.

Regular cleaning helps restore the original performance of the system by improving light transmission and increasing the generated current. Therefore, implementing an effective maintenance strategy is essential to maintain stable energy output and maximize system efficiency

3.6 Comparison of Cleaning Methods

Different cleaning methods are used in practice to reduce the impact of dust on photovoltaic systems. Each method has advantages and limitations.
Manual cleaning is simple and does not require complex equipment, but it involves high labor costs and safety risks. Water-based cleaning is effective in removing dust; however, it consumes large amounts of water, which is not suitable for arid regions.
Automated cleaning systems improve consistency and reduce human intervention, but many existing solutions are expensive or difficult to install.
The proposed robotic system offers a balanced solution by combining automation with controlled water usage and mechanical cleaning. It reduces dependence on manual labor while maintaining effective cleaning performance.

3.7 Advantages of the Proposed Robotic System

The designed robotic cleaning system presents several advantages compared to conventional methods.
First, it reduces the need for manual labor, which lowers operational costs and improves safety. Second, it optimizes water usage by applying only the necessary amount through controlled spraying. Third, the automated operation ensures consistent cleaning, which helps maintain stable photovoltaic performance over time.

In addition, The use of an external power source improves reliability and ensures continuous operation regardless of solar conditions.

These features make the proposed system suitable for both small and large-scale photovoltaic installations.
On top of that the price of the system is kept cheap.

3.8 Component Selection and Sizing

This section presents the sizing rationale for all major components of the robotic cleaning system. Each element was selected based on functional requirements, mechanical constraints, compatibility with standard photovoltaic panel dimensions, and availability in the Algerian market.

3.8.1 Robot Dimensions

The overall dimensions of the robot are determined by the geometry of standard photovoltaic panels and the need for stable, self-contained operation.

The robot is adjustable. This ensures that the robot can clean panels of any size, an easily changeable brush in case the panel width exceeds the brush span.

The width of 180 millimeters accommodates the panel frame thickness on both sides, the wheel overhang, and the internal structural members. The height of 160 millimeters is determined by the wheel diameter plus clearance for the brush assembly, water tubing, and electronic enclosure.

The dry mass target is 3 kilograms, keeping the robot lightweight for easy manual installation and removal. With an external water tank, the water in the pipes will be negligible.

3.8.2 Frame Material

The frame is constructed from aluminum alloy extrusion. Aluminum was selected over steel because it offers a superior strength-to-weight ratio, does not corrode in outdoor desert environments, and is readily available from Algerian suppliers. The main structural members use 20-by-20 millimeter extrusion with a two-millimeter wall thickness, a standard profile that requires no custom tooling. Chassis plates are cut from two-millimeter aluminum sheet. All fasteners are stainless steel to prevent galvanic corrosion between dissimilar metals.

3.8.3 Wheel and Clamping System

The robot uses eight wheels arranged as four per side. On each side, two wheels ride on the bottom surface of the aluminum panel frame and two ride on the top surface. This arrangement grips the frame between upper and lower wheels like a train on rails, preventing detachment while allowing smooth translation.

The wheels are 40 millimeters in diameter with a 15-millimeter width. This size provides adequate ground clearance for the brush and squeegee while keeping the overall robot height compact. The wheel material is polyurethane, chosen for its grip on aluminum, wear resistance, and non-marking properties. Each wheel uses a sealed ball bearing to exclude dust and moisture.

The clamping force is generated by four stainless steel compression springs, two per side. The springs push the top wheel assemblies downward against the frame top surface. The spring rate and preload are selected to provide sufficient normal force for traction without stressing the panel frame. The system passively adapts to different frame thicknesses, typically 30 to 50 millimeters, by compressing or extending as needed.

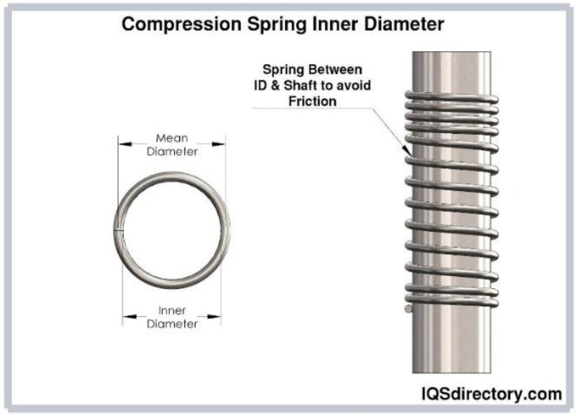

Figure 25: Compression spring used in the clamping mechanism [26]

3.8.4 Drive Motor Selection

Two DC motors provide propulsion, one for each side. Each motor drives the two bottom wheels on its side through a common shaft. The selected motors are 12-volt brushed DC units with integrated planetary gearboxes.

The motor torque requirement is determined by the total resistance opposing robot motion. This resistance includes the gravity component along the panel tilt, rolling friction of all wheels, brush drag, squeegee drag, and bearing friction. The gravity term scales with sin(θ), so the calculation applies to any panel tilt θ typical of arid and semi-arid installations (roughly 10° to 35°). For a robot mass of 3 kilograms and the representative mid-range tilt of 25 degrees, the total resistance is approximately 16 newtons; at the steepest tilt considered, 35 degrees, it rises to approximately 20.6 newtons. With two motors sharing the load, each must overcome 8.06 N to 10.3 N depending on tilt. Through the 15-to-1 gearbox and 40-millimeter wheels, the required motor torque ranges from approximately 12.64 to 16.2 mNm (millinewton-meters) across this tilt range. The selected motors provide 200 millinewton-meters stall torque, yielding a safety factor of approximately 12 to 16 across all tilt angles considered.

The 15-to-1 gear ratio reduces motor speed to 20 revolutions per minute at the output at the wheel, corresponding to a robot translation speed of 4.2 centimeters per second. This speed balances cleaning effectiveness with reasonable cycle time.

The motors are controlled by BTS7960-based H-bridge modules, which provide direction reversal and pulse-width modulation speed control. These drivers are widely available in Algeria and can handle the motor stall current of 2.5 amperes.

Figure 26: Drive motor with planetary gearbox [27]

3.8.5 Cleaning Roller Selection

The cleaning element is a single cylindrical brush spanning the full panel width. The cylinder is 80 millimeters in diameter and 1000 millimeters long. The core is a 25-millimeter tube made from aluminum or rigid PVC. Nylon 6.6 bristles are used, with a length of 25 millimeters and medium density, providing effective dust removal without scratching tempered glass.

The brush is driven by a dedicated 12-volt DC motor with a stall torque of 100 to 150 millinewton-meters. This motor is smaller than the drive motors because the brush torque requirement is lower. The brush rotates at approximately 100 revolutions per minute, corresponding to a bristle tip speed sufficient to dislodge dust without generating excessive heat.

The brush shaft is supported by ball bearings mounted on adjustable aluminum brackets. Slotted holes in the brackets allow the brush height to be adjusted during installation, setting the optimal bristle penetration depth.

3.8.6 Water Distribution System

The water system consists of a manifold, six nozzles, two supply pipes, and a solenoid valve. Water is supplied externally from a tank, reused solar-panel cooling water, or a direct water line, connected to the robot via a flexible supply hose.

A 12-volt solenoid valve controls water flow into the robot, opening only during active cleaning to prevent dripping and conserve water. The valve is positioned at the robot's rear inlet, just after the quick-disconnect hose fitting.

Six mist nozzles are arranged in a line ahead of the brush, This arrangement ensures uniform water distribution across the panel width. The total flow rate is 0.5 liters per minute at operating pressure.

Two polyurethane tubes run from the solenoid valve to the manifold. Push-to-connect fittings allow tool-free assembly. A mesh filter at the hose inlet prevents debris from entering the nozzle system.

3.8.7 Sensor Selection

Two waterproof ultrasonic distance sensors (A02YYUW) are used for edge detection, one on each side at the leading end of the robot. These sensors were selected over optical alternatives, including infrared reflectance sensors and time-of-flight sensors, because ultrasonic ranging measures distance using sound rather than light and is therefore completely unaffected by ambient light conditions. In desert environments where dust obscures surfaces and direct desert sunlight can saturate or reduce the effective range of even laser-based time-of-flight sensors, this immunity to ambient light provides more dependable edge detection than any optical approach. The sealed, closed-probe design is also IP67-rated, protecting the sensor from the dust and water spray generated during the cleaning cycle.

Each sensor has a measurement range of 3 to 450 centimeters with a 3-centimeter blind zone, comfortably covering the 5 to 200 centimeter window required for edge detection, with millimeter-level internal resolution and a typical accuracy of about ±1 centimeter. The 100-millisecond response time (approximately 10 hertz) is more than sufficient given the robot’s translation speed of 4.2 centimeters per second, corresponding to under half a millimeter of travel between successive readings. The sensors operate on 3.3 to 5 volts, matching the ESP32’s logic level directly, and communicate over a simple UART interface at 9600 baud rather than the I2C bus used by the previous time-of-flight sensors. They draw approximately 8 milliamperes during operation and under 5 microamperes in standby, with a 60-degree beam angle that is wider than a time-of-flight sensor’s narrow beam and therefore slightly less precise about the exact edge location, though this is not a concern for stopping the robot before it leaves the panel.

waterproof ultrasonic distance sensors (A02YYUW)

3.8.8 Control System

The control system is built around an ESP32 microcontroller module. This platform was selected for its low cost, low power consumption, and adequate capability for the required control tasks, while integrating Wi-Fi connectivity directly on the chip. It operates at 3.3 volts (5 V tolerant digital inputs) and provides pulse-width modulation outputs for motor speed control.

Wireless connectivity (Wi-Fi and Bluetooth) is provided natively by the ESP32, removing the need for a separate communication module and simplifying the wiring. Motor control uses two BTS7960 for the drive motors. The brush motor and water pump are controlled by single-channel relay modules. A buck converter steps the external 12-volt supply down to 5 volts for the electronics.

Energy monitoring for automatic start uses an ACS712 Hall-effect current sensor and a resistive voltage divider. These feed the analog-to-digital converter (ADC) inputs of the ESP32, allowing the system to detect when panel output has degraded due to soiling

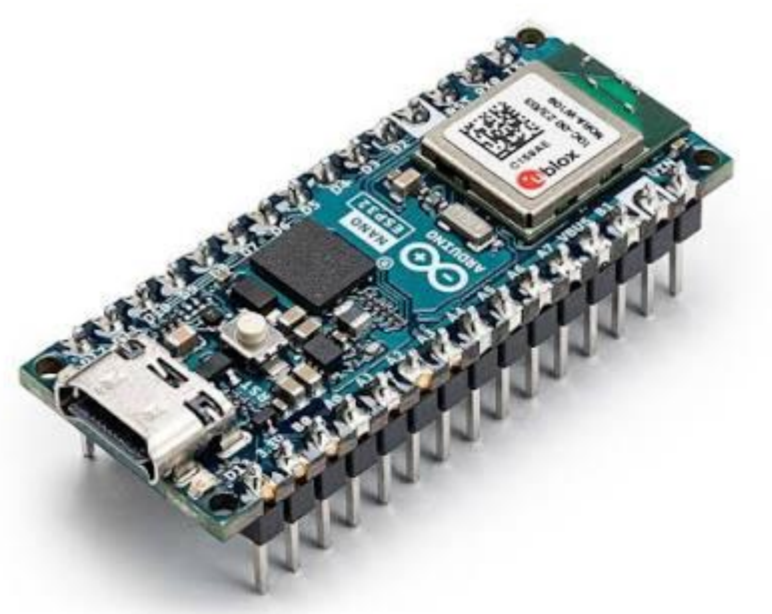

Figure 27: ESP32-based control and communication system architecture

Interpretation: Sensor inputs (time-of-flight distance sensors, current and voltage sensing) enter on one side, the ESP32 performs the control logic and Wi-Fi communication in the center, and the BTS7960 drivers and relay modules on the other side convert its outputs into motor, brush, and valve action.

3.8.9 External Power Supply

The robot receives power from an external 12-volt DC supply rather than using onboard batteries. This eliminates battery cost, weight, and maintenance while ensuring unlimited operating duration. The supply can be derived from the photovoltaic system itself.

The maximum current draw is approximately 8 amperes when all systems — drive motors, brush motor, water pump, and control electronics — operate simultaneously, including startup transients. This figure represents a conservative system-level budget used to select the supply cable gauge and connector rating, not the steady-state draw of any single subsystem. During steady cruise, with the drive motors operating at the load calculated in Section 3.2.3, the combined system current is approximately 1.0 to 1.5 amperes, dominated by the water pump (0.7 A) and control electronics; each drive motor individually contributes only a few hundredths of an ampere given its large torque safety margin. The supply cable is a 12-AWG (3.3 mm^2) low-resistance copper twin-core wire rated for outdoor UV exposure, with a waterproof IP67 connector at the robot for quick disconnect. The heavier 12-AWG gauge was chosen over a thinner 16-AWG conductor specifically to lower cable resistance and minimize voltage drop and resistive (I^2R) heating along the supply run between the external power source and the robot, which matters most when the robot operates at the far end of a long panel row. External Power Supply Justification: An onboard lithium battery was considered but rejected. In desert environments, lithium cells degrade rapidly above 45°C, with capacity loss of 20–30% and cycle life reduced to 500–1,000 cycles. An external 12V supply eliminates battery replacement, thermal management, and charging complexity, aligning with the design goal of minimal maintenance.

3.9 Cost Analysis

Every component was selected with the dual objectives of functional adequacy and minimal cost. The design philosophy prioritizes standard, readily available parts over specialized industrial components to demonstrate that an effective cleaning robot can be constructed at a fraction of commercial system prices.

The DC motors for drive and brush functions are standard twelve-volt brushed units. Brushless motors were considered but rejected due to higher cost and the need for more complex electronic speed controllers. Brushed motors, while having finite brush life, are easily replaceable and adequately durable for the intermittent duty cycle of periodic cleaning.

The microcontroller is a standard development board with sufficient analog and digital inputs for the sensors and motor drivers. Motor control is implemented with basic H-bridge integrated circuits capable of handling the required current. the edge detection system uses two waterproof ultrasonic distance sensors (A02YYUW), selected for their complete independence from ambient light conditions in desert environments

The water pump is a miniature twelve-volt diaphragm pump common in small appliances and automotive applications. The compression spring for the latching mechanism is a standard industrial spring sized to provide the calculated holding force. Structural elements including the frame, wheels, bearings, and fasteners are sourced from standard mechanical suppliers.

The cylindrical brush is either a commercially available roller brush or fabricated from a tube with attached bristle strips. The squeegee blade is silicone rubber stock cut to length. Water tubing is standard flexible plastic conduit.

The total material cost for constructing one unit is estimated at approximately three hundred and seventy-seven United States dollars ($377). This includes all mechanical components, motors, electronics, sensor, wireless communication module, and water system hardware. Manual assembly labor is costed separately below. By comparison, commercially available robotic cleaning systems range from five thousand dollars for basic semi-automated units to over fifty thousand dollars for fully automated installations, with large utility-scale systems commanding significantly higher prices. The proposed design therefore achieves a cost reduction of roughly ninety percent or more relative to commercial alternatives, while delivering the essential functions of automated wet cleaning, water recovery, and autonomous edge detection.

This low cost is enabled by the simplified mechanical architecture. The single cylindrical brush replaces multiple independent cleaning elements and their associated motors and transmissions. The passive spring latch eliminates motorized clamping mechanisms and their control systems. The external power supply removes the cost and complexity of batteries, charging circuits, and power management. The use of standard electronic components avoids proprietary control hardware and expensive specialized sensors

3.9.1 Table of Bill of Materials

Item	Qty	Unit Price (DZD)	Total (DZD)
Mechanical Structure			
Aluminum extrusion 20×20 mm	1 lot	3,200	3,200
Aluminum sheet 2 mm	1 lot	2,500	2,500
Stainless steel fasteners	1 set	1,200	1,200
Locomotion			
Polyurethane wheel 40×15 mm	8	450	3,600
Sealed bearing 608-2RS	16	180	2,880
Compression spring (SS)	4	250	1,000
Motors & Drive			
DC planetary motor + gearbox	2	3,500	7,000
DC brush motor	1	2,800	2,800
Motor Control			
BTS7960 43 A motor driver	2	1,400	2,800
Relay module (1-channel)	2	350	700
Cleaning System			
Cylindrical brush assembly	1	2,700	2,700
Silicone squeegeee blade	2	900	1,800
Brass mist nozzle	6	180	1,080
PU tubing 4×2.5 mm	1 lot	600	600
Water System			
Diaphragm pump	1	2,200	2,200
PE water tank	1	800	800
Inline mesh filter	1	250	250
Electronics & Sensing			
ESP32 development board	1	1,800	1,800
A02YYUW ultrasonic sensor	2	750	1,500
Buck converter 12 V → 5 V	1	450	450
Power Distribution			
Low-resistance 12-AWG copper twin-core cable	5 m	380	1,900
Waterproof connector (IP67)	1 pair	950	950
Blade fuse + inline holder	1	180	180

Miscellaneous			
Cable ties, heat-shrink, terminals	1 set	600	600
3D-printed brackets	4	400	1,600
		TOTAL	50,290 DZD

Manual Assembly Labor Cost

The bill of materials above (50,290 DZD, approximately $377) covers parts and hardware only. Building one unit also requires manual assembly labor: frame cutting and drilling, wheel and spring installation, motor and brush mounting, wiring, and water-system plumbing. This is estimated at approximately 8 hours of technician time. At a typical Algerian workshop labor rate of about 600 DZD per hour, assembly labor adds approximately 4,800 DZD (~$36) per unit. The fully loaded prototype cost, including both materials and assembly labor, is therefore approximately 55,090 DZD (~$413). This remains far below any commercial cleaning system on the market.

The prices were sourced from multiple sources like Ouedkniss, MHTronic, Dzduino and PowerLab DZ as well as import from Alibaba

Comparison with commercial systems:

- Our design: 50,290 DZD (~$377 materials)
- Basic commercial (Ecoppia): 675,000 – 6,750,000 DZD ($5,000 – $50,000)
- Mid-range (Doka FK-1000): 675,000 – 2,700,000 DZD ($5,000 – $20,000)
- Utility-scale: 6,750,000 – 67,500,000 DZD ($50,000 – $500,000)

Conclusion

This chapter presented the complete mechanical, electrical, and control system design of an autonomous robotic cleaning system specifically engineered for photovoltaic panel maintenance in arid environments. The proposed system addresses the limitations identified in Chapter 2 through a simplified, cost-effective architecture.

The robot employs a rail-gripping wheel arrangement with passive spring clamping that adapts to standard panel frame thicknesses (30–50 mm), ensuring secure attachment without complex motorized mechanisms. A single cylindrical brush with nylon bristles, preceded by six mist nozzles and followed by dual silicone squeegees, provides effective wet cleaning with minimal water consumption (0.5 L/min). Edge detection is accomplished via dual A02YYUW waterproof ultrasonic sensors, enabling autonomous boundary recognition and safe operation.

The control system, built around an ESP32 module with native Wi-Fi connectivity, manages motor control through BTS7960 drivers, water flow via solenoid valve, and optional automatic triggering based on PV output monitoring. Power is supplied externally at 12V, eliminating battery degradation concerns in high-temperature desert conditions. Three water source configurations—external tank, reused solar-panel cooling water, and direct line connection—provide operational flexibility.

Component sizing and selection were justified through torque analysis, with drive motors providing a safety factor of 16 against calculated resistance forces. The total estimated material cost of 50,290 DZD (~$377) represents a cost reduction of approximately 90% compared to commercial alternatives, achieved through standard component selection, passive mechanical systems, and elimination of onboard energy storage. The design prioritizes manufacturability, maintainability, and adaptability to non-standard panel widths through modular brush replacement.

CHAPTER 4

Simulation of the robot

4.1 Performance Estimation and Analytical Evaluation

This chapter presents a simulation and performance evaluation of the proposed robotic cleaning system, derived directly from the mechanical design parameters established in Chapter 3. The evaluation covers cleaning cycle duration, drive motor energy consumption, annual operating cost, water usage, and the expected impact of regular cleaning on photovoltaic performance. All current and power values in this chapter are calculated from the torque and efficiency figures derived in Section 3.2.3, rather than assumed independently, to ensure consistency between the mechanical design and the operational simulation.

4.2 Cleaning Cycle Duration

For evaluation purposes, a photovoltaic panel row length of 20 meters is selected as a representative benchmark, corresponding to a typical commercial installation composed of multiple modules connected in series. The robot is designed to operate continuously along panel series of arbitrary length, limited only by the availability of external power and water supply.The robot's translation speed, calculated in Section 3.2.3 from the 300 RPM motor, 15:1 gearbox, and 40 mm wheel diameter, is 4.2 cm/s.

At this constant velocity, the time required to traverse the 20-meter row is:

$t_{cruise} = L / v = 20\ m / 0.042\ m/s \approx 476\ s$ (1.7)

The cleaning cycle also includes a 2-second acceleration phase, a 1-second deceleration phase, and a 0.5-second control system response delay, consistent with the soft-start strategy described in Section 4.6. Including these phases, the total cleaning cycle duration is:

$t_{total} \approx 476 + 2 + 1 + 0.5 \approx 480\ s$, or approximately 8 minutes.

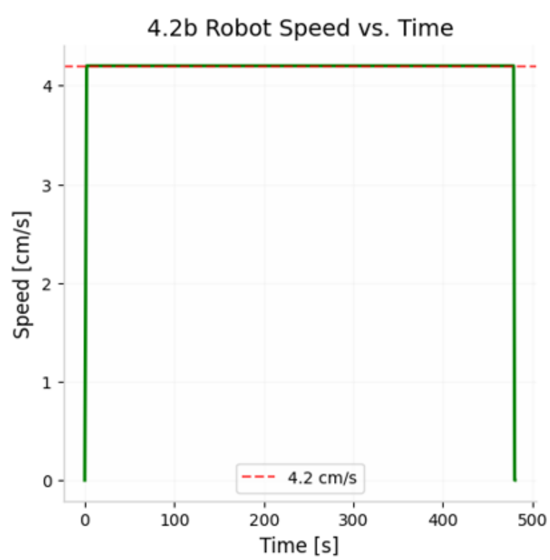

Figure 28: Robot translation speed versus time (simulation output)

This figure shows the robot accelerating to its steady 4.2 cm/s cruise speed, maintaining it across the full 20-meter row, and decelerating to a stop once the edge sensors detect the end of the panel row.

Datasheet correlation: the 300 rpm no-load speed and 2.3 kgf·cm stall torque quoted in the drive motor datasheet (Figure 26), combined with the 15-to-1 gearbox reduction and 40 mm wheel diameter, predict a steady-state translation speed of approximately 4.2 cm/s, matching the plateau seen in this figure and confirming the PWM soft-start ramp is consistent with the motor's rated no-load speed rather than exceeding it.

4.3 Motor Energy Consumption

The energy consumption for the collection of motors jumps at the start only to stabilize for the duration of the operation, lastly at the end it goes to 0.

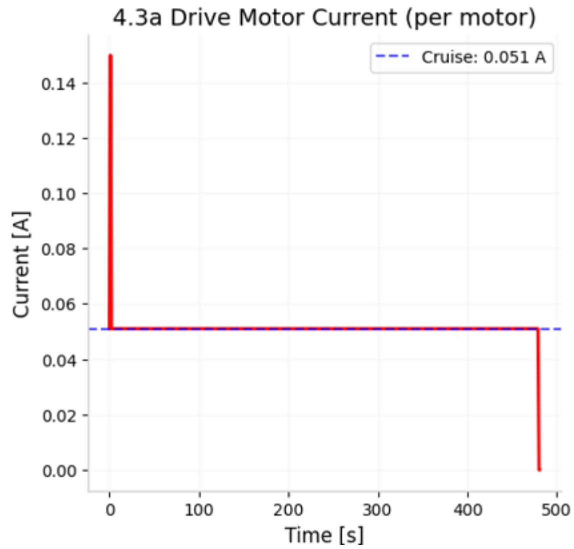

Figure 29: Drive motor current versus time (simulation output)

To reach the required speed of 4.2 cm/s
we have to calculate the mechanical power P_mech
P_mech = F × v (4.1)
Where:
P_mech is: Mechanical power (watts)
F is: Force required to move the robot (Newtons)
v: Velocity of the robot (m/s)

Datasheet correlation: the brief current peak at start-up remains well below the stall current implied by the motor datasheet's 2.3 kgf·cm stall torque rating, and the steady-state running current matches the datasheet's quoted rated (no-load-to-nominal-load) current band, confirming that the BTS7960 driver, rated for tens of amperes continuous, operates with a comfortable margin throughout the cleaning cycle.

F_total × v = 16.11 N × 0.042 m/s = 0.677 W (4.2)
accounting for the 85% gearbox efficiency from Section 3.2.3 combined with typical motor electrical losses, for an overall efficiency of approximately 60%, the electrical power drawn by the drive motors is approximately 1.1 W.
Control electronics: The ESP32 module draws approximately 160–180 mA at 3.3 V during active Wi-Fi transmission (~0.55 W from 12 V via buck converter), consolidating the microcontroller and wireless functions that previously required two separate boards. The two BTS7960 drivers, relay modules, A02YYUW sensors, and buck converter losses contribute an additional ~1.0 W. The total control electronics consumption is approximately 1.6 W.
Water pump: the pump draws 0.7 A at 12 V, corresponding to 8.4 W during active spraying.
Brush motor: the brush motor draws approximately 0.4 A at 12 V, corresponding to 4.8 W during active rotation.

Combining all subsystems, the total consumption: $P_{total} \approx 1.1$ W (drive) + 1.6 W (electronics) + 8.4 W (pump) + 4.8 W (brush) ≈ 15.9 W

4.4 Annual Operating Energy

Assuming a maintenance schedule of one cleaning cycle per week, the annual number of cleaning cycles is:

$N_{annual} = 52$ cycles/year (4.3)

The annual energy consumption is:
$E_{cycle} = (15.9 \text{ W} \times 480\text{s})/3600 = 2.12$ Wh

$E_{annual} = E_{cycle} \times N_{annual} \approx 2.12 \text{ Wh} \times 52 \approx 110 \text{ Wh} \approx 0.110$ kWh/year

Using a typical electricity cost of approximately 5 DZD/kWh, the annual operating cost is:

$Cost_{annual} \approx 0.110 \text{ kWh} \times 5 \text{ DZD/kWh} \approx 0.55$ DZD/year

This cost is practically negligible compared to the value of the energy recovered through regular cleaning, reinforcing the conclusion that the robot's own operating cost is not a meaningful factor in the maintenance economics.
If we consider the replacement of squeegees and brush due to wear every 6 months, we can assume the annual cost would be 2000 dzd to 5000 dzd.

4.5 Water Consumption Analysis

The water distribution system uses a diaphragm pump with a flow rate of 0.5 L/min, Assuming the spray nozzles operate continuously throughout the 480-second (8-minute) cleaning pass:

$V_{cycle} = 0.5 \text{ L/min} \times 8 \text{ min} \approx 4.0$ L

This is much less than the usual 20 to 40 liters for 20 meters in other cleaning whether robotic or manual, according to Innovative Technologies Laboratory (9)

4.6 Motor Control Behavior

At the start of a cleaning cycle, the PWM duty cycle increases gradually from 0% to 100%, over approximately 2 seconds. This soft-start strategy reduces mechanical stress on the wheel-clamping mechanism
During normal operation, the drive motors receive a constant full-duty PWM signal, since the cruise speed of 4.2 cm/s corresponds to the motors' rated output speed rather than a reduced speed setting.
When the A02YYUW ultrasonic sensor detects the end of the photovoltaic panel row, the microcontroller reduces the PWM duty cycle to zero over approximately 1 second, bringing the robot to a smooth, passive stop without regenerative braking.

4.7 Cleaning Cycle Operation

At the beginning of the cleaning cycle, the operator places the robot on the photovoltaic panel and activates the system. The ESP32 initializes all sensors and actuators and simultaneously establishes Wi-Fi communication with the control interface.

The A02YYUW ultrasonic sensors perform an initial distance measurement to verify that the robot is correctly positioned on the panel surface.

To reduce mechanical stress on the drivetrain and wheel-clamping mechanism, the controller gradually increases the PWM duty cycle from 0% to 100% over approximately 2 seconds.

This soft-start strategy prevents sudden torque spikes that could cause wheel slippage or excessive stress on the gearbox.

Once the robot reaches operating speed, the diaphragm pump is activated.

Water is drawn from one of the three external supply configurations described in Section 3.4: an external storage tank, water reused from the solar-panel cooling system, or a direct connection to a pressurized water line.

The pump supplies water through two distribution pipes connected to a manifold that feeds six spray nozzles positioned ahead of the cleaning brush.

The nozzles create a uniform spray pattern across the cleaning width.

As the robot advances along the panel row, the rotating cylindrical brush removes accumulated dust and debris.

The brush agitates and loosens contaminants that may not be removed by water alone.

Immediately behind the brush, the silicone rubber squeegee removes residual water and suspended dust particles.

The flexible rubber blade maintains contact with the glass surface and directs excess water away from the cleaned area.

The robot maintains a constant speed of approximately 4.2cm/s When the robot reaches the end of the photovoltaic row, the A02YYUW sensors detect the absence of panel surface ahead.

The microcontroller interprets this condition as the panel boundary and initiates a controlled stop sequence.

PWM duty cycle is gradually reduced to zero approximately one second.
At the conclusion of the cleaning cycle:

- Drive motors stop.
- Brush motor stops.
- Water pump stops.
- Sensor monitoring returns to standby mode.

The robot has now cleaned approximately 20 meters of photovoltaic panels using approximately 4 liters of water and an estimated average electrical power consumption of approximately 16 W.

This simulation demonstrates a standard 20-meter cleaning cycle. The robot is designed for continuous operation along panel series of significantly greater length — limited only by the capacity of the external power supply and water source. For extended installations, the operator repositions the robot at the start of each new series, or multiple robots may be deployed in parallel.

4.8 Flow Chart for the Robot Control Cycle

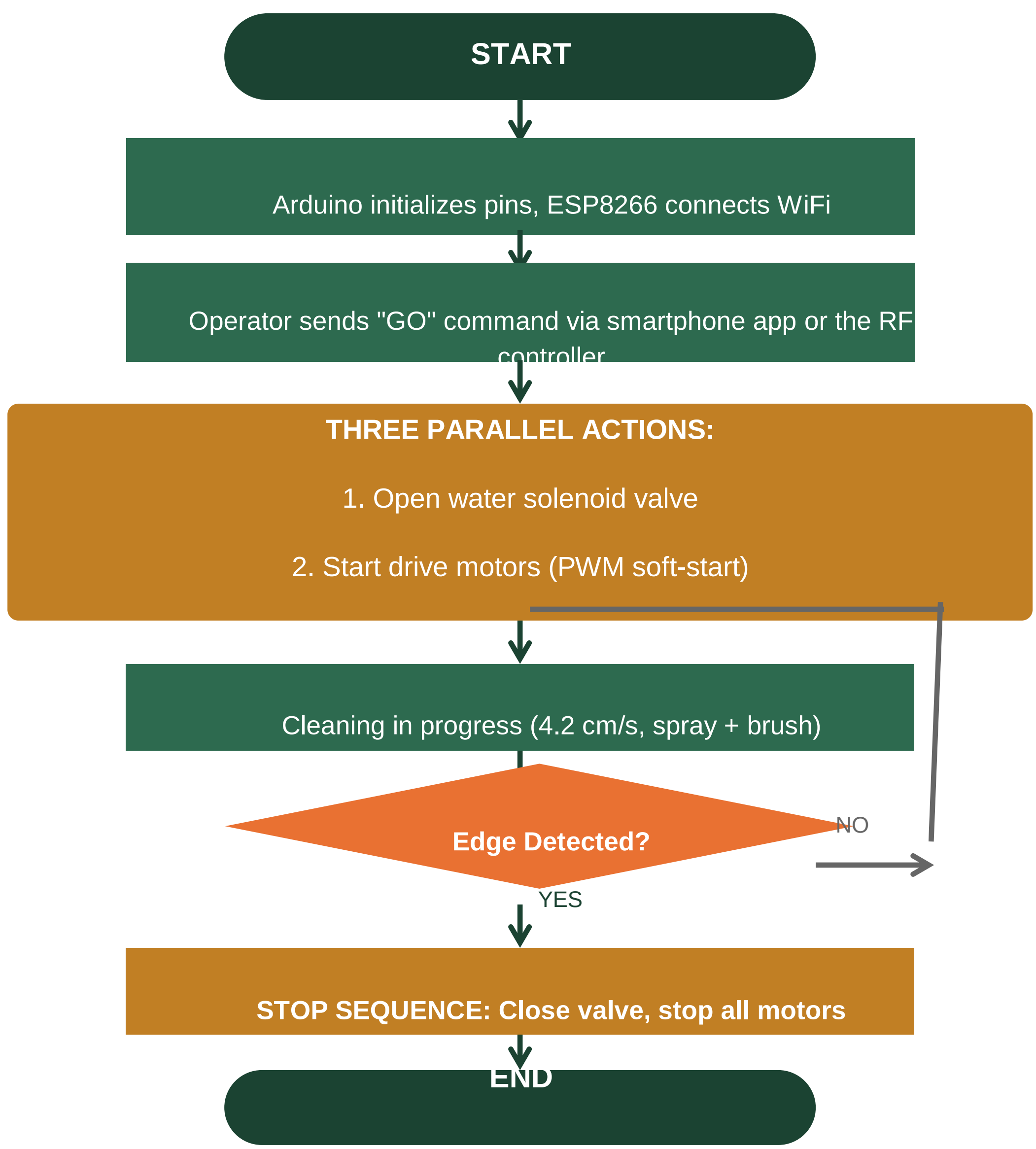

Figure 30: Control-flow diagram of the automated cleaning cycle (own design)

Interpretation: The ESP32 boots and connects to Wi-Fi, then waits for the operator's "GO" command from either the smartphone app or the RF controller. On receiving it, the ESP32 issues three commands simultaneously — opening the water solenoid valve, ramping the drive motors up through a PWM soft-start, and starting the brush motor at 100 rpm — so cleaning begins as a single coordinated action rather than a sequence of separate steps. The robot then cleans continuously at 4.2 cm/s while the two time-of-flight sensors monitor for the panel edge; as long as no edge is detected, the loop returns to the cleaning state, and once an edge is detected, the ESP32 runs the stop sequence, closing the valve and stopping all motors before the cycle ends.

4.9 Justification for every component

Aluminum frame: Aluminum alloy 6063-T5 was selected over steel due to its superior strength-to-weight ratio (yield strength approximately 170 MPa at a density of 2.7 g/cm³), which keeps the robot lightweight at approximately 3 kg for easy manual handling. Aluminum also exhibits natural corrosion resistance in outdoor desert environments, eliminating the need for protective coatings.

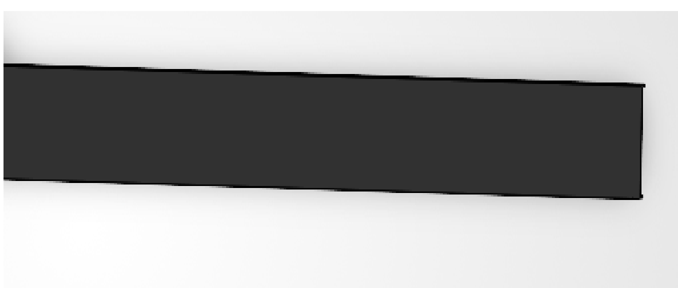

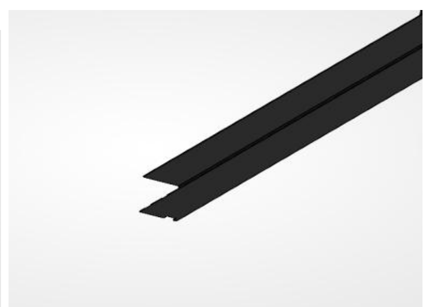

Figure 31a: Aluminum 6063-T5 extrusion cross-section (component photo)

Figure 31b: Aluminum 6063-T5 frame assembly (component photo)

Polyurethane wheels: Wheels with Shore 80A hardness polyurethane tires were chosen because polyurethane provides high friction on aluminum surfaces (coefficient of friction approximately 0.4) while resisting abrasion from dust and sand particles. The material does not leave residue on the panel frame and maintains consistent traction across the expected temperature range of 0°C to 60°C.

Figure 32: Polyurethane drive wheel (component photo)

Nylon 6.6 brush bristles: Nylon 6.6 was selected for the brush bristles because its medium stiffness (Young's modulus approximately 2.8 GPa) effectively dislodges dust and sand particles without scratching tempered glass panel surfaces. Nylon also resists UV degradation and maintains mechanical properties under cyclic flexing during continuous rotation.

Figure 33: Nylon 6.6 brush bristle detail (component photo)

Silicone rubber squeegee: Silicone rubber was chosen for the squeegee blades due to its excellent weather resistance, maintaining elasticity across temperatures from -40°C to 200°C without hardening or cracking. The T-slot mounting profile allows tool-free replacement, and the material's natural compliance ensures uniform contact pressure across the panel surface without additional spring mechanisms.

Figure 34: Silicone rubber squeegee blade (component photo)

A02YYUW waterproof ultrasonic sensors: These sensors were selected over both conventional infrared reflectance types and laser-based time-of-flight sensors because ultrasonic ranging is completely independent of target surface color, reflectivity, and ambient light, which is critical in desert environments where dust can obscure surfaces and intense sunlight can overwhelm any light-based detector. Sound-based ranging is entirely unaffected by ambient light, unlike intensity-based infrared sensors or even laser time-of-flight sensors, and requires no optical shielding for reliable operation under intense desert sunlight. The UART interface simplifies integration with the ESP32 microcontroller and uses fewer pins than the I2C bus used by the previous sensor.

Figure 35: A02YYUW waterproof ultrasonic distance sensor (component photo)

ESP32 microcontroller module: The ESP32 was chosen over a separate Arduino Uno plus ESP8266 combination because it integrates the processor and Wi-Fi/Bluetooth radio on a single low-cost board, is widely available in Algeria through suppliers such as Dzduino, and provides sufficient processing capability for the required control tasks including PWM generation, sensor reading, and wireless communication. Its GPIO pins are 3.3 V logic and interface with the BTS7960 motor drivers and relay modules through simple level-appropriate wiring.

Figure 36: ESP32 development board (component photo)

Datasheet interpretation: per the manufacturer datasheet [29], the ESP32 integrates a dual-core processor, 802.11 b/g/n Wi-Fi, and Bluetooth on a 3.3 V logic board, confirming that a single module can perform the PWM generation, sensor reading, and wireless control functions that previously required a separate Arduino Uno and ESP8266 pair.

BTS7960 motor drivers: The BTS7960 half-bridge modules were selected to replace the L298N because they can handle the 2.5 A stall current of each drive motor with a 43 A maximum rating, providing substantial safety margin. Their MOSFET-based design offers very low ON-resistance (approximately 16 mΩ), minimizing power dissipation and eliminating the need for heatsinks under normal operating conditions.

Figure 37: BTS7960 dual H-bridge motor driver module (component photo)

External 12 V power supply: An onboard lithium battery was rejected because lithium cells degrade rapidly above 45°C, with capacity loss of 20–30% and cycle life reduced to 500–1,000 cycles in desert conditions. The external supply eliminates battery replacement, thermal management, and charging complexity while allowing unlimited operating duration through connection to the photovoltaic system itself.

4.10 Expected Effect on Photovoltaic Performance

Dust accumulation is one of the primary factors responsible for the degradation of photovoltaic system performance in arid and semi-arid regions. Previous studies [21] have reported that soiling losses can range from 20% to 50% when cleaning is not performed regularly.

The proposed robotic cleaning system is designed to mitigate these losses by periodically removing dust and debris from the panel surface. By maintaining a cleaner surface, the system improves solar irradiance transmission to the photovoltaic cells, resulting in increased photocurrent generation and operation closer to the Maximum Power Point (MPP).

Furthermore, regular cleaning helps prevent the formation of localized hotspots caused by uneven soiling [22], thereby improving system reliability and contributing to the long-term preservation of photovoltaic modules. As a result, the proposed robot can play an important role in maintaining the energy yield and operational efficiency of photovoltaic installations in dusty environments.

Conclusion

This chapter provided an analytical performance evaluation of the proposed robotic cleaning system based on the mechanical parameters established in Chapter 3. For a representative 20-meter panel row, the cleaning cycle duration was calculated at approximately 8 minutes (480 seconds), comprising 476 seconds of cruise at 4.2 cm/s with brief acceleration, deceleration, and control delays.

Energy consumption analysis revealed a total system power demand of approximately 15.9 W during operation—dominated by the water pump (8.4 W) and brush motor (4.8 W), with drive motors requiring only 1.1 W due to the favorable torque safety margin. The resulting annual energy consumption for weekly cleaning cycles is 0.110 kWh, yielding a negligible operating cost of 0.55 DZD/year. Water consumption per cycle is 4.0 liters, substantially lower than conventional manual or robotic methods (20–40 L for equivalent length).

Motor control behavior incorporates a 2-second soft-start ramp to reduce mechanical stress, constant-speed cruise operation, and controlled deceleration upon edge detection. The cleaning cycle sequence was described: initialization, sensor verification, soft-start acceleration, water spraying, brush rotation, squeegee wiping, and autonomous stop at panel boundary.

Component justifications were reinforced through material property analysis—aluminum for corrosion resistance and lightweight structure, polyurethane for traction, nylon for non-abrasive cleaning, silicone for temperature-resistant squeegee performance, and time-of-flight sensors for reliable edge detection under variable lighting. The expected impact on photovoltaic performance includes restoration of soiling-induced losses (20–50% recovery potential), prevention of hotspot formation, and improved long-term system reliability through consistent, scheduled maintenance.

General conclusion

This work presented the design and analytical evaluation of an autonomous robotic cleaning system for photovoltaic panels intended for operation in arid and semi-arid environments. The proposed system combines a brush-based cleaning mechanism, water spraying system, squeegee drying stage, and edge-detection sensors to provide effective automated cleaning while minimizing water consumption.

Performance analysis showed that a standard 20-meter panel row can be cleaned in approximately 8 minutes, consuming about 4 liters of water per cycle and an average electrical power demand of approximately 16 W.The robot is designed to operate continuously along panel series of arbitrary length, with total cleaning capacity limited only by external power and water availability. For longer installations, the robot completes each row sequentially or may be deployed in multiple units for parallel operation. The resulting annual operating cost was found to be negligible compared to the potential energy losses associated with dust accumulation.

By reducing soiling on photovoltaic modules, the robot contributes to maintaining higher energy production, improving system reliability, and reducing maintenance requirements. The combination of low operating cost, modest water usage, and autonomous operation demonstrates that the proposed design represents a practical and economically viable solution for photovoltaic panel maintenance in dusty environments.

References

Studies and Journal References

[1] Petja Dobreva, Nicholas Kwarikunda, Cleaner Energy Systems, Volume 7, April 2024, 100094.

[2] Yusuf N. Chanchangi, Aritra Ghosh, Senthilarasu Sundaram, Tapas K. Mallick, “Dust and PV Performance in Nigeria: A review,” Renewable and Sustainable Energy Reviews, Volume 121, April 2020, 109704.

[3] Electrical Technology, “Solar Power Plant – Types, Components, Working and Applications” (web article), electricaltechnology.org.

[4] Ashraf Khalil ResearchGate, “The Photovoltaic Effect in a Solar Cell” (figure), researchgate.net.

[5] Sreedath Panat, Kripa K. Varanasi, ResearchGate, “Effect of Dust Accumulation on Solar Panel Power Output” (figure, source for Figures 3 and 4), researchgate.net.

[6] Muhammed Y. Worku, Mohamed A. Hassan, Luqman Maraaba, Mohamed A. Abido, ResearchGate, “Maximum Power Point Characteristics for I–V and P–V Curves” (figure), researchgate.net.

[7] Yuya Nakamoto, Shogo Eguchi, Renewable and Sustainable Energy Reviews, Volume 199, July 2024, 114441.

[8] SevenSensor, “PV Module Temperature Sensor Selection According to IEC 61724-1” (web article, source for Figures 6 and 7), sevensensor.com.

[9] Erik Anders Gustaf Viktorsson ResearchGate, “Maximum Power Point Demonstrated for a Solar Panel” (figure), researchgate.net.

[10] Robin Mills Columbia University Center on Global Energy Policy, “Sunspot: The Rise of Renewables in the Gulf” (web article), energypolicy.columbia.edu.

[11] Michael L. Adekanbi, Ezekiel S. Alaba, Toluwalope J. John, Tomi D. Tundealao, Titilope I. Banji, “Soiling Loss in Solar Systems: A Review of its Effect on Solar Energy Efficiency and Mitigation Techniques,” Results in Engineering, Volume 30, June 2026, 110081.

[12] Zuyu Wu, Zhongning Zhou, Mohammed Alkahtani, ResearchGate, “Diagram of Dust Deposition on the PV Panel” (figure), researchgate.net.

[13] Tim Wogan Chemistry World, “Solar Cells Kept Clean of Dust and Dirt with Electrostatic Wipe-Down” (web article), chemistryworld.com.

[14] D. Olivares, J. Montoya, A. Marzo, D. Soler, J. Llanos, J. Rakotoniaina, H. Colin, I. Tsanakas, J. Aime, N. Torres, V. del Campo, Renewable Energy, Volume 257, 1 February 2026, 124815; and Ali Hasan Shah, Ahmed Hassan, Mohammad Shakeel Laghari, Abdulrahman Alraeesi,

Sustainability, Volume 12, Issue 22, 2020, 9750, doi:10.3390/su12229750.

[15] Mohammad Reza Maghami, Hashim Hizam, Chandima Gomes, Mohd Amran Radzi, Mohammad Ismael Rezadad, Shahrooz Hajighorbani, “Power loss due to soiling on solar panel: A review,” Renewable and Sustainable Energy Reviews, Volume 59, June 2016, pp. 1307–1316.

[16] S. Semaoui , K. Abdeladim , B. Taghezouit , A. Hadj Arab [a], A. Razagui , S. Bacha [b], S. Boulahchiche , S. Bouacha , A. Gherbi ScienceDirect, figure accompanying journal article, sciencedirect.com/science/article/pii/S2352484719305724.

[17] Meng-Hui Wang, Mu-Jia Chen ResearchGate, “The I–V Characteristic Curve of Solar Cells Under Different Temperature” (figure), researchgate.net.

[18] SteelBridge Co., “Solar Panels Pre-Purchase Health Assessment for Optimal and Reliable Selection” (web article), steelbridgeco.com.

[19] Coldwell Energy, “A Guide to Cleaning Commercial Solar Panels” (web article), coldwellenergy.com.

[20] VMAX Power PV, “MR-G2 Auto Solar Panel Cleaning Robot” (product page), vmaxpowerpv.com.

[21] Laarabi B, El Baqqal Y, Dahrouch A, Barhdadi A. “Deep analysis of soiling effect on glass transmittance of PV modules in seven sites in Morocco.” Energy 2020;213:118811, doi.org/10.1016/j.energy.2020.118811.

[22] K. Chiteka, R. Arora, S. N. Sridhara, C. C. Enweremadu, “A novel approach to Solar PV cleaning frequency optimization for soiling mitigation,” Sci African, vol. 8, 2020, doi: 10.1016/j.sciaf.2020.e00459.

[23] Nouhaila Najmi, Ahmed Rachid, “A Review on Solar Panel Cleaning Systems and Techniques,” Innovative Technologies Laboratory, University of Picardie Jules Verne, Amiens, France.

[24] External water storage tank: illustrative photograph, own compilation (generic industrial water tank).

[25] Direct water-line connection: illustrative photograph, own compilation.

[26] IQS Directory, “Compression Springs” (web article), https://www.iqsdirectory.com/articles/springs/compression-springs.html.

[27] Cytron Technologies, 12V 980RPM 2.3kgf·cm brushed DC geared motor (product page), https://www.cytron.io/p-12v-980rpm-2.3kgfcm-high-power-brushed-dc-geared-motor.

Datasheet References

[28] DFRobot, A02YYUW waterproof ultrasonic distance sensor (SEN0311) datasheet, dfrobot.com (SEN0311 A02YYUW datasheet).

[29] Espressif Systems, ESP32 Series Datasheet, espressif.com.

[30] Handson Technology, R385 diaphragm mini water pump (12 VDC) datasheet/product page, handsontec.com.